Nano Today 27 (2019) 99–119

Contents lists available at ScienceDirect

Nano Today

journal homepage: www.elsevier.com/locate/nanotoday

Review

Electrically tunable physical properties of two-dimensional materials

Xiaolong Chen [a,*], Zishu Zhou [b], Bingchen Deng [c], Zefei Wu [d], Fengnian Xia [c], Yi Cao [b], Le Zhang [a], Wei Huang [b,e], Ning Wang [d], Lin Wang [b,*]

[a] Department of Electrical and Electronic Engineering, Southern University of Science and Technology, Shenzhen, 518055, China
[b] Key Laboratory of Flexible Electronics (KLOFE) & Institute of Advanced Materials (IAM), Jiangsu National Synergetic Innovation Center for Advanced Materials (SICAM), Nanjing Tech University (Nanjing Tech), 30 South Puzhu Road, Nanjing, 211816, China
[c] Department of Electrical Engineering, Yale University, 15 Prospect St Becton 519, New Haven, Connecticut, 06511, USA
[d] Department of Physics, the Hong Kong University of Science and Technology, Hong Kong
[e] Shaanxi Institute of Flexible Electronics (SIFE), Northwestern Polytechnical University (NPU), 127 West Youyi Road, Xi'an, 710072, Shaanxi, China

ARTICLE INFO

Article history:
Received 6 February 2019
Received in revised form 29 March 2019
Accepted 21 May 2019
Available online 15 June 2019

Keywords:
Two-dimensional material
Electrically tunable property
Electro-matter interaction

ABSTRACT

Two-dimensional (2D) materials, with atomically thin van der Waals layered structure, exhibit both novel physical properties and promising applications in electronic, optoelectronic and energy-harvesting devices. Currently 2D material research has become one of the most exciting topics in physics, engineering and material communities due to the easy preparation processes, rich species and unique properties. Among all the unique properties of 2D materials, the ability to electrically tune the electronic, optical and even magnetic properties at a mild electrostatic doping offers us numerous possibilities for investigating electro-matter interactions and novel device applications. Here, we review the electrically tunable physical properties of several interesting 2D materials as well as the relevant applications on devices utilizing these unique properties. The electrically tunable valley properties of 2D materials and the recent discovered 2D magnetism are also included.

Contents

* Corresponding authors.
E-mail addresses: chenxl@sustech.edu.cn (X. Chen), iamlwang@njtech.edu.cn (L. Wang).

https://doi.org/10.1016/j.nantod.2019.05.005
1748-0132/

Introduction

The discovery of graphene in 2004 [1,2], an atomically thin carbon material, has overturned the traditional cognition that two-dimensional (2D) materials cannot be stabilized in ambient. Since then, various 2D materials with novel physical properties have been brought into our sight, including the family of transition-metal dichalcogenides (TMDs) [3–5], hexagonal boron nitride (hBN) [6,7], black phosphorus (BP) [8,9], etc. They can be categorized as metals, semimetals, semiconductors, insulators, topological insulators and superconductors.

Today, 2D materials in general are no longer restricted to monolayer forms and are referred to the materials with layered structures where layers are held together through van der Waals (vdW) interactions. Hence 2D materials are also called layered materials or vdW materials. A recent high-throughput computational research has shown that 5619 compounds are in layered structure, and among them 1825 compounds are easily or potentially exfoliable [10]. Thus, the abundant species of 2D materials provide a vast platform for investigating both novel physical properties and new functional devices. For example, monolayer graphene shows an unconventional half-integer quantum Hall effect [1,11,12], TMDs pave the way for valley-physics and valleytronics [13], and quantum spin Hall insulators are theoretically modeled and predicted in a strong spin-orbit coupling graphene lattice [14]. The layered magnetic materials uncovered recently, push forward the understanding of 2D magnetic phases and development of spintronics [15]. Besides, vdW heterostructures [16,17], a stack of different atomically thin 2D materials through vdW interactions, bring us new opportunities for realizing novel functional devices, such as vertical transistors [18–20], tunneling light emitting diodes [21–23], photodetectors [24–26], memory devices [27–29], etc.

Because of the atomically thin nature of 2D materials, their physical properties are very sensitive to external environments and can be conveniently controlled and tuned through various approaches. For example, the physical properties of 2D materials strongly depend on the layer number (thickness). With increasing layer numbers, graphene evolves from a Dirac semimetal for monolayer to a metallic material for bulk [30], 2H-MoS_2 shows a direct to indirect bandgap transition from monolayer to bilayer [4,31], and the bandgap of BP gradually decreases from $\tilde{2}$ eV in monolayer to $\tilde{0}.3$ eV in bulk [8,9]. An in-plane compressive or tensile strain can also be used to tune the physical properties of 2D materials, especially their electronic band structures [32]. The strain will induce pseudo-magnetic fields [33–35], tune the bandgap size [36,37], induce direct to indirect bandgap transitions [36,37], and even result in structural phase transitions [38].

Another widely used and convenient way to tune the physical properties of 2D materials is through purely electrical approaches, such as the electrical gating [39]. Compared with other approaches, the electrical tuning method shows various advantages. For example, the electrical tuning of physical properties shows a much faster speed than that of mechanical strain, and the electrical tuning unit can be conveniently integrated on chip in micro/nanometer scale. The electrical tuning approach has already been used in many aspects of electronics and optoelectronics. For example, the field-effect transistors [39–41], the fundamental unit of modern electronic circuits, are realized through electrical switching of carrier transport to achieve on and off states. The light-emitting diodes [42,43], one of the most important and indispensable technologies in our daily life, are also controlled electrically to tune the brightness and spectra. As the dielectric screening effect is much reduced in 2D materials due to the atomically thin nature [44–46], a mild electric field can result in a very dramatic change in the physical properties of 2D materials compared with conventional materials. Hence, 2D materials could offer us a new platform for investigating both fundamental electro-matter interactions and novel functional devices.

Here, we summarize the electrically tunable physical properties of 2D materials. Due to the abundant species of 2D materials, we mainly focus on several representative materials, including bilayer graphene, BP, TMDs (MoS_2, $MoTe_2$, TaS_2, and WTe_2), and emerging layered magnetic materials, such as CrI_3 and Fe_3GeTe_2 (see Fig. 1). We discuss the electrically tunable electronic properties, such as the gate-tunable band structures, structural phase transitions, transport metal-insulator transitions (MIT) and tunable ferroelectric properties; the electrically tunable optical properties, such as tunable optical conductivity, photoresponse and excitons; the electrically tunable magnetic properties, including electric field-induced magnetic phase transitions and tunable spin transport. We also discuss the electrically tunable valley properties of graphene and TMDs. The device applications utilizing the electrically tunable physical properties of 2D materials are also included.

Field effect and carrier doping effect

Field effect and carrier doping effect are key physical mechanisms widely used for electrically tuning the physical properties of 2D materials. Here, we use graphene, the most investigated and well-known 2D material, as an example to illustrate these two effects [1,2].

Fig. 1b shows the most common device configuration for utilizing the field effect. It is a parallel-plate capacitor structure with metallic materials (such as highly doped silicon) as one electrode of the capacitor, oxide or hBN as insulating layer, and graphene (or other 2D materials) as the other electrode. This structure has been widely used in the fundamental building unit of modern electronics, the metal-oxide-semiconductor (insulated-gate) field-effect transistors, which is known as MOSFET (IGFET) [39–41]. Through applying a positive (negative) gate voltage V_g on silicon, electron (hole) carriers will be induced in graphene as a result of the field effect (Fig. 1c), which is also called the electrostatic doping effect. Due to the Pauli exclusion principle, the density of states of electrons is finite at different Fermi energy. Hence the filling of carriers in Fermi energy induced by the gate voltage will shift the position of Fermi level. Compared with bulk materials, 2D materials show lower density of states and weak screening effect, and thus the Fermi level tuning effect is more pronounced. Especially for graphene, its linear energy-momentum dispersion (known as Dirac cone as shown in Fig. 1c) ensures an ultra-low density of states near the Dirac point [30]. The associated electronic and optical properties of graphene, such as density of states, electrical conductivity and optical absorption, can be widely tuned by gate

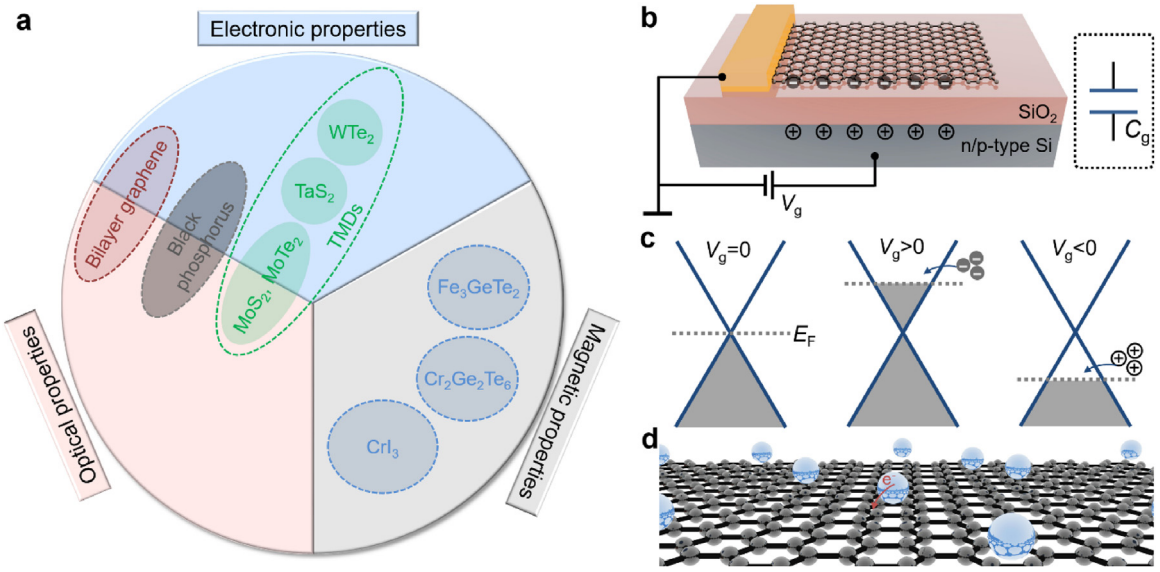

Fig. 1. (a) Electrically tunable physical (electronic, optical and magnetic) properties of representative two-dimensional (2D) materials that are included in this review, such as bilayer graphene, TMDs (MoS_2, $MoTe_2$, TaS_2, and WTe_2), black phosphorus (BP), CrI_3 and Fe_3GeTe_2. (b) Insulated-gate field-effect structure for electrically tuning the physical properties of 2D materials. (c) The Fermi level position of intrinsic monolayer graphene as a function of gate voltage V_g. (d) Schematics showing the carrier doping effect induced by the charge transfer from foreign atoms to 2D materials.

Table 1
Merits and disadvantages of field effect using insulated gate structure, field effect using ion liquid, and carrier doping by foreign atoms.

Doping method	Carrier density (cm^{-2})	Reversibility	Device applications
Field effect-insulated gate	10^{13} cm^{-2}	Reversible	Suitable
Field effect- ion liquid	>10^{14} cm^{-2}	Reversible	Not suitable
Foreign atoms	>10^{14} cm^{-2}	Irreversible	Not suitable

voltage V_g under the field effect structure [1,11,30,47]. Since there are abundant reviews on the physical properties and applications of graphene [2,5,12,30,48], they will not be the focus of this review.

The carrier doping density induced by the field effect using insulated-gate structure is usually at order of 10^{13} cm^{-2} limited by the breakdown voltage of insulator. In some situations, higher carrier doping density is required to observe the tunable physical properties, and ion liquid are usually used as gating materials [49,50]. Because an ionic double layer (thickness is around 1 nm) is formed on material surface, the gating capacitance is very high, leading a carrier doping density over 10^{14} cm^{-2} [49,50].

Another method to electrically tune the physical properties of 2D materials is through carrier doping by foreign atoms. As illustrated in Fig. 1d, foreign atoms, such as potassium (K), are deposited on to graphene surface without destroying its crystalline structure (the ionic bond are formed between foreign atoms and graphene instead of the covalent bond) [51]. Charges will transfer from foreign atoms to graphene, shift the Fermi level of graphene, and tune the properties of graphene. Compared with the electrostatic doping through field effect, the carrier doping density induced by foreign atoms can be one or two orders higher. However, the carrier doping effect induced by foreign atoms is irreversible, and is not suitable for device applications. In Table 1, we summarized the merits and disadvantages of field effect using insulated gate structure, field effect using ion liquid, and carrier doping by foreign atoms.

Bilayer graphene

Electric-field induced bandgap and device applications

Bilayer graphene consists of two monolayer graphene sheets in Bernal-stack (AB-stack) as shown in Fig. 2a. Each unit cell of bilayer graphene contains four carbon atoms resulting in four electronic bands in momentum space (see Fig. 2b). Distinguished from the linear energy-momentum dispersion in monolayer graphene [1,11,52], the lower energy bands in bilayer graphene touch with quadratic dispersion due to layer-to-layer coupling [30,53]. This leads to many unique physical properties in bilayer graphene, such as the massive chiral quasiparticles at Dirac point and the unconventional integer quantum Hall effect [12,53,54]. Besides, the double layer nature of bilayer graphene offers another degree of freedom to control the lattice symmetry and associated physical properties.

In 2006, McCann and Fal'ko [55,56] have theoretically shown that an energy difference between two layers could lead to a sizable energy bandgap in bilayer graphene (Fig. 2b). This prediction is soon confirmed via various experimental techniques, including angle-resolved photoemission spectroscopy (ARPES) [57], transport measurement [58–61], infrared spectroscopy [62,63], electron compressibility [64,65] and photocurrent measurement [66].

The most effective and convenient approach to introduce an energy difference in graphene bilayer is through electrostatic doping [59–67]. This can be realized by constructing a metal/insulator/bilayer-graphene/insulator/metal dual-gate structure [59–66] as shown in Fig. 2c. By tuning the top gate (V_{tg}) and back gate (V_{bg}) voltages, an electrostatic displacement field ($D = \frac{\varepsilon_b V_{bg}}{d_b} - \frac{\varepsilon_t V_{tg}}{d_t}$) is induced across the bilayer graphene, where ε_b (d_b) and ε_t (d_t) are the dielectric constant (thickness) of top and back gate insulators, respectively. This results in an energy difference between two layers, depending on the displacement field and graphene interlayer thickness. At the same time, the carrier density ($n = \frac{\varepsilon_b V_{bg}}{ed_b} + \frac{\varepsilon_t V_{tg}}{ed_t}$) can be tuned continuously, where e is the elementary charge. Hence, the dual-gate configuration is more flex-

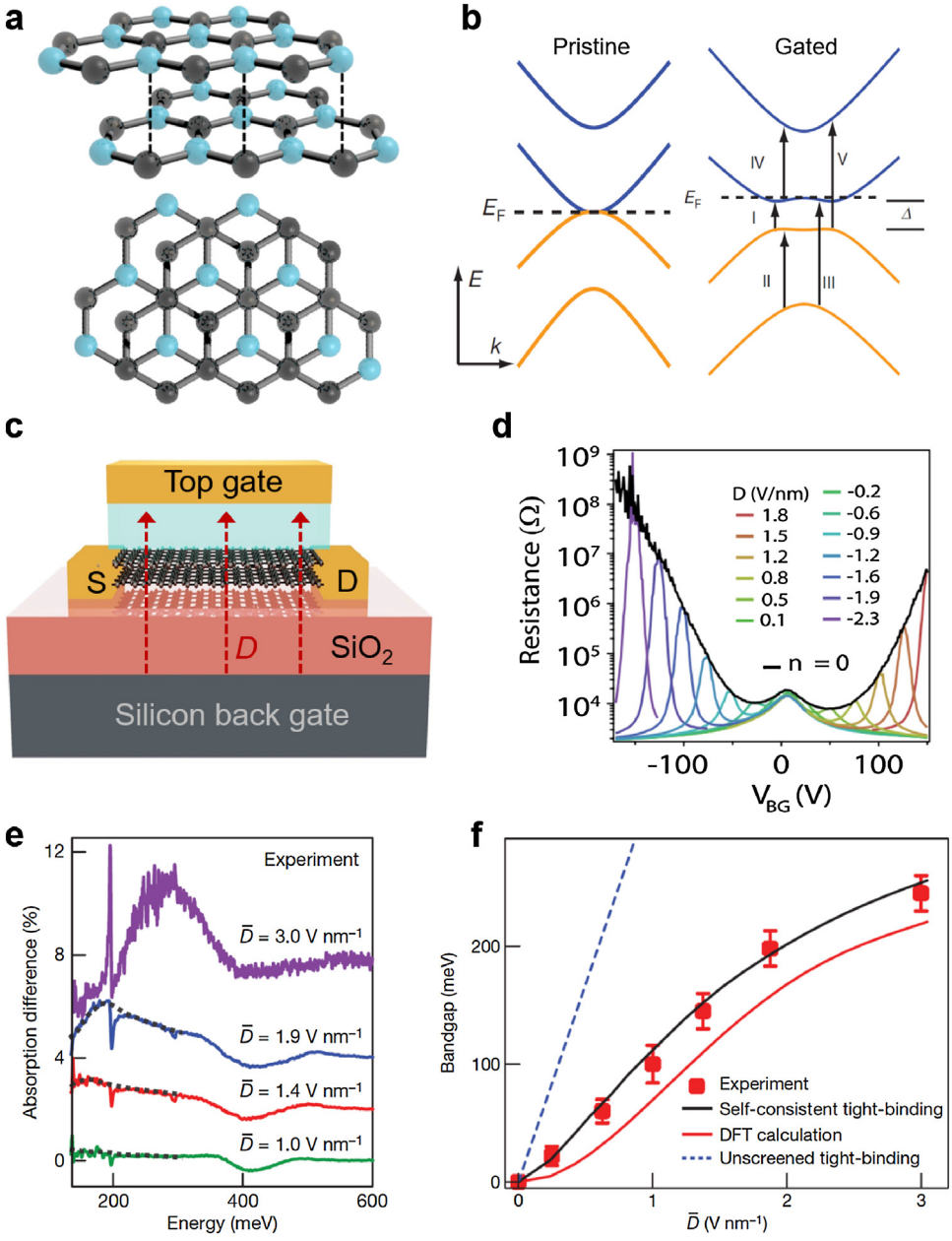

Fig. 2. Electric-field induced bandgap in bilayer graphene. (a) Perspective side and top views of bilayer graphene lattice. (b) Electronic band structure of pristine (left panel) and gated bilayer graphene with gap opening (right panel). Reproduced with permission [62]. Copyright, 2009, Nature Group Publishing. (c) Schematic image of a dual-gate bilayer graphene transistor. The amplitude and direction of the displacement field D are controlled through top and back gate voltages. (d) Resistance of bilayer graphene as function of back gate voltages at different displacement fields. Reproduced with permission [61]. Copyright, 2010, American Physical Society. (e) The optical absorption spectra of bilayer graphene at various displacement fields. Reproduced with permission [62]. Copyright, 2009, Nature Publishing Group. (f) Electric-field tunable bandgap in bilayer graphene. Reproduced with permission [62]. Copyright, 2009, Nature Publishing Group.

ible and controllable compared with the chemical doping method [57].

In 2008, Oostinga et al. first studied the transport properties of bilayer graphene at different displacement fields using the dual-gate field-effect transistor (FET) configuration [59]. Fig. 2d shows a typical transport characteristics of bilayer graphene at different displacement fields [61]. The resistance at charge-neutrality point (at carrier density $n = 0$) is significantly larger at higher displacement field, indicating an energy gap opening. At low temperature (< 70 K), the resistance at higher displacement field shows insulating behavior and was explained based on variable range hopping (VRH) and nearest-neighbor hopping (NNH) mechanisms, consistent with the electron behavior inside an energy gap [59,61].

A more direct approach to confirm the energy gap opening in bilayer graphene is through optical absorption measurements [62,63]. Under the optical excitation, several optical transitions occur inside the four energy bands of bilayer graphene (process I to V shown in Fig. 2b). Zhang et al. studied the optical absorption in bilayer graphene with displacement fields up to 3 Vnm^{-1} (Fig. 2e). At strong displacement fields (>1.2 V nm^{-1}), the transition I from upper valence band to lower conduction band can be directly observed by monitoring the optical absorption spectrum. The absorption peak position directly corresponds to the optical bandgap size of bilayer graphene. However, at weak displacement fields (< 1.2 V nm^{-1}), the transition I is too weak to be detected. Instead, the optical bandgap can be studied through monitoring

the absorption spectra of transition II to V [62,63]. As shown in Fig. 2f, at a moderate displacement field of 1 V nm^{-1}, a reasonable bandgap size of 100 meV is achieved [62].

The gap opening in bilayer graphene has enabled many novel applications in electronics and optoelectronics. In 2010, Xia et al. demonstrated a dual-gate bilayer graphene FET with current on-off ratio over 100 at room temperature and 2000 at 20 K with gap opening [60]. Then Szafranek et al. showed that bilayer graphene FETs exhibited an intrinsic voltage gain up to 35 at a displacement field of 1.7 V nm^{-1}, 6 times higher than that in monolayer graphene FETs [67], revealing promising applications in radio frequency electronics, terahertz technology and infrared optoelectronics. In 2012, Yan et al. demonstrated a dual-gate bilayer graphene hot-electron bolometer operating from visible to mid-infrared region ($\tilde{1}$0.6 μm), taking advantage of the large temperature-dependent electron conductivity inside the energy gap [68]. The bolometer exhibits a low noise-equivalent power of 33 fW $Hz^{-1/2}$ at 5 K and an intrinsic high speed at order of GHz, which outperforms commercial silicon bolometers operating at similar temperatures [68].

Electrically tunable valley properties and valley valves

Electronic valleys, in energy band theory, refer to the energy extrema located in momentum space. Inequivalent valleys, well separated in the Brillouin zone, can be energetically degenerate due to symmetry and serve as novel information carriers controllable via external electric fields. In 2006, Mansour Shayegan's group first proposed the concept of manipulating valleys in AlAs 2D electron systems, where they successfully changed the valley population and accessed the value of valley susceptibilities by applying a strain to the system [69–71]. Later in 2007, Rycerz et al. proposed a graphene quantum-point-contacted nanodevice using the valley degree of freedom [72].

2D material with hexagonal lattice provides an ideal platform to study valley physics [13]. Unlike valleys in other traditional materials (e.g., silicon [73], aluminum arsenide [69,70]), valleys in 2D hexagonal lattice are easily addressed, manipulated, and measured [72,74–76]. This is because there are observable physical quantities affiliated to different valleys [77,78]. For example, in the absence of the lattice inversion symmetry, graphene was predicted to support valley currents due to the non-vanishing Berry curvatures Ω with same magnitude but opposite signs for K and K' valleys [77]. In 2014, Gorbachev et al. were able to detect the valley currents in graphene superlattices through coupling graphene with a hBN substrate [79]. At the graphene-hBN vdW-interface, a superlattice (periodic Moiré pattern) is formed due to the lattice mismatch. As a result, the lattice inversion symmetry of graphene is broken, giving rise to the non-vanishing Berry curvatures at K and K' valleys [79].

A vertical electric field not only modulates the bandgap of bilayer graphene, but also its valley properties [80–82]. Intrinsic bilayer graphene has preserved inversion symmetry, and Berry curvature is zero all across the momentum space. However, when a vertical electric field is applied to a bilayer graphene, the system becomes inversion symmetry broken and a finite bandgap emerges [62]. Fig. 3a shows the low energy band structure of gapped bilayer graphene [81]. Two sets of energy-degenerate while inequivalent electronic valleys K and K' are clearly denoted by different colors. Therefore, in the first Brillouin zone, carriers not only carry spin indices but also valley indices. Similar to spin, valley is another degree of freedom in 2D hexagonal lattice, and it is also expected to store, manipulate, and carry information [69–72,83–85]. In this case, non-trivial Berry curvature hot spots appear in K and K' valleys. Because the K and K' valleys are time-reversal copies of each other, the Berry curvatures associated with them are of opposite polarities [13,80,81]. Fig. 3a (right panel) also shows the Berry curvature Ω and the consequent (valley) Hall conductivity σ_{xy}^{VH} as a function of Fermi energy [81]. Utilizing their different Berry curvatures, it is feasible to distinguish carriers with different valley indices by practical physical measurements. Berry curvature, in short, is a pseudo-magnetic field in momentum space [86]. In real space, carriers with opposite charge signs curve to different directions in the presence of a magnetic field, which is the well-known Hall effect. In momentum space, carriers with opposite valley indices curve to different directions due to the opposite pseudo-magnetic fields (Berry curvatures) they experience. Translating to real space, carriers in different valleys gain opposite transverse velocities, which is schematically shown in Fig. 3b [79]. Here, carriers are separated by their valley indices, not charge signs, and the phenomenon is called the valley Hall effect (VHE). In gapped bilayer graphene, VHE has been measured due to its non-trivial Berry curvature distribution in momentum space [13,80,81]. What is more, it is largely tunable because of its tunable bandgap and the associated valley properties. Fig. 3c shows the non-local measurement scheme to detect valley current in gapped bilayer graphene [81]. Here, VHE does not distinguish carriers with different charge signs, therefore non-local scheme needs to be applied, instead of conventional Hall effect configuration. Besides VHE, carriers in different valleys also manifest themselves in other aspects. They carry different angular momenta, therefore it is possible to address them by circularly polarized light, namely, left (right) circularly polarized light can only excite carriers in K (K') valley [77]. Bilayer graphene thus offers an opportunity to realize tunable valleytronics, combing with mid-infrared optoelectronics.

The bilayer graphene AB-BA domain walls also support the one-dimensional (1D) chiral valley currents (Fig. 3d) [87–89]. In 2015, this chiral valley currents were experimentally detected in dual-gate bilayer graphene transistors with AB-BA domain walls [90]. Although the bilayer domain walls are robust for 1D chiral valley currents, the seek for such domain walls is a very challenging work. In 2016, Li et al. developed a dual-split-gate structure in bilayer graphene (Fig. 3e) and showed strong evidence of the topological valley currents [91]. By tuning the bilayer graphene to the insulating region through controlling the two pairs of split-gates, a line junction (quasi-1D channel) is formed between the two split-gates. In the 'odd' field configuration (electric field directions of the split gates are opposite as shown in Fig. 3e), there are four conducting modes for each valley propagating along the line junction (two for spins and two for layer numbers). Similar to the chiral edge states in the quantum Hall effect, the topological protection of the valley strongly suppresses any valley-mixing mechanisms and results in the robust 2D chiral valley currents [91]. Based on this concept, Li et al. further demonstrated a valley valve with an current on-off ratio of 8 at zero magnetic field in 2018 [92]. As illustrated in Fig. 3g, through tuning the polarity of split-gates, the propagation of valley currents is controlled, acting as a current waveguide. The device can also work as a coherent electron-beam splitter with the presence of a magnetic field [92].

Electrically tunable excitons

Exciton, a quasiparticle formed by Coulomb interactions between an electron and a hole, is an important physical quantity of semiconductors [93–95]. It can be excited by optically pumping an electron from valence band to conductance band in a semiconductor. The left hole in valence band will interact with the electron in conductance band and form an exciton. In low dimensional materials, the reduced Coulomb screening effect will enhance the electron-hole interactions and lead to a larger binding energy, which can be experimentally resolvable. Although the exciton has been well studied in various two-dimensional systems, such as semiconducting TMDs [96–100] and BP [101–103], it has not been

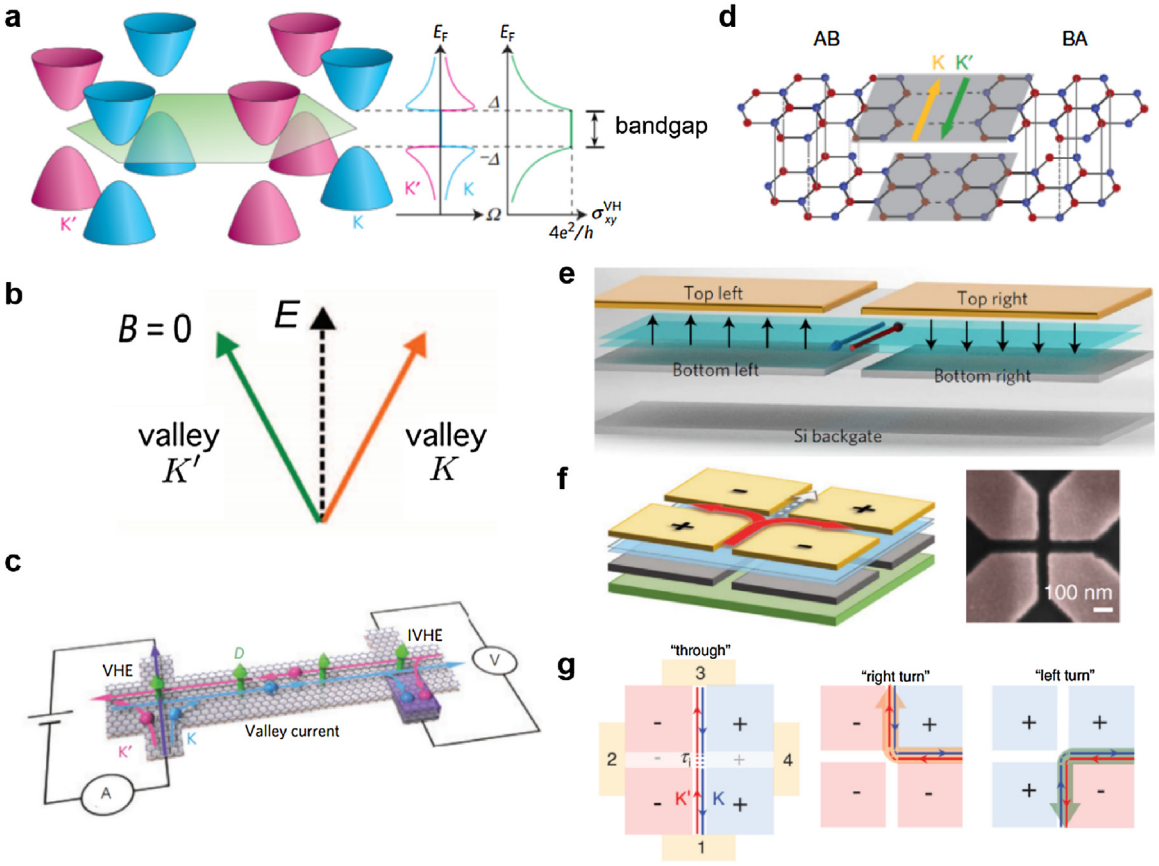

Fig. 3. Electrically tunable valley properties in bilayer graphene. (a) Left panel: the band structure of gapped bilayer graphene. K (K') valleys are denoted by blue (red) colors. Right panel: Berry curvature Ω and valley Hall conductivity σ_{xy}^{VH} are plotted as a function of Fermi level E_F, for K and K' valleys. Reproduced with permission [81]. Copyright, 2015, Nature Publishing Group. (b) Schematic of valley Hall effect (VHE). Under a drift current, K valley carriers and K' valley carriers have opposite transverse velocity components, even in the absence of a magnetic field. Reproduced with permission [79]. Copyright, 2014, American Association for the Advancement of Science. (c) Schematic of non-local measurement to detect VHE in bilayer graphene. From the driving arm (left side), due to VHE, carriers in K and K' valleys are separated. Through the pure valley current transport to the detection arm (right side), due to the inverse valley Hall effect (IVHE), the valley current is converted back to charge current and therefore results in a non-local voltage drop. Reproduced with permission [81]. Copyright, 2015, Nature Publishing Group. (d) Schematic of the AB–BA domain wall in bilayer graphene. The arrows indicate the topological one-dimensional (1D) valley current at the domain wall from K- (yellow) and K'-valley (green). Reproduced with permission [90]. Copyright, 2015, Nature Publishing Group. (e) Schematic of the dual-split-gate structure in bilayer graphene. The black arrow indicates the electric field induced by top and back gate biases. If the electric fields under two split gates have same (opposite) directions, the system is in even (odd) configuration. Reproduced with permission [91]. Copyright, 2016, Nature Publishing Group. (f) Schematic (left panel) and SEM (right panel) images of the bilayer graphene valley valve and electron beam splitter. The electric field direction from bottom to top gates is indicated by "+". Reproduced with permission [92]. Copyright, 2018, American Association for the Advancement of Science. (f) Configuration of the gate-controlled waveguide for the propagation of kink states. Reproduced with permission [92]. Copyright, 2018, American Association for the Advancement of Science.

observed in gapped bilayer graphene due to challenging device fabrication and measurement techniques.

In 2017, Ju et al. reported the observation of excitons in bilayer graphene using photocurrent measurement based on a modified Fourier transform infrared spectroscopy [66]. The bilayer graphene preserves its high quality and intrinsic properties through sandwiching into thin hexagonal boron nitride (hBN) layers. Thin graphite bottom gate and transparent NiCr top gate are used to tune the electric field across bilayer graphene. In the photocurrent spectroscopy, two pronounced exciton peaks P1 and P2 are observed (Fig. 4a) [66]. The excitons can be widely tuned from terahertz frequency to mid-infrared region by adjusting the electric field D across bilayer graphene (Fig. 4b) [66].

The origin of exciton P1 and P2 is quite unusual compared with conventional semiconductors. In conventional semiconductors, such as GaAs quantum wells [104], the exciton s states are bright whereas the p states are dark subject to the selection rules. In contrast, due to the presence of valley-dependent pseudospin with winding number of 2 in bilayer graphene, the exciton angular momentum would acquire a value of ± 2 (see Fig. 4c), resulting in dark exciton s states and bright p states [66]. The high energy peak P2 arises from the bright exciton p state, while the low energy peak P1 originating from the exciton s state is not completely dark, because of the slightly rotation symmetry breaking near K and K' valley points [66].

Black phosphorus

Black phosphorus (BP), the most stable form of allotrope of phosphorus, was first synthesized by P.W. Bridgman in 1914 through converting white phosphorus at a high pressure [105]. One century later, BP was rediscovered as a 2D layered semiconductor and much attention is focused on its monolayer, few-layer, and thin film forms [106–111]. As shown in Fig. 5a, the semiconducting BP has a puckered orthorhombic lattice, resulting in anisotropic electronic and optical properties. For example, the charge carriers have higher carrier mobility, larger drift velocity, and smaller effective mass along the armchair (x) direction [106–108,112–117], the optical absorption is much stronger when light polarization is along the armchair direction [107,118,119], and the photoluminescence linearly polarized along the armchair direction in monolayer and few-layer BP [101–103]. Distinguished from TMDs, BP is a direct bandgap semiconductor at all thickness. The bandgap size covers the spectrum from visible to mid-infrared regime, depending on the thickness of

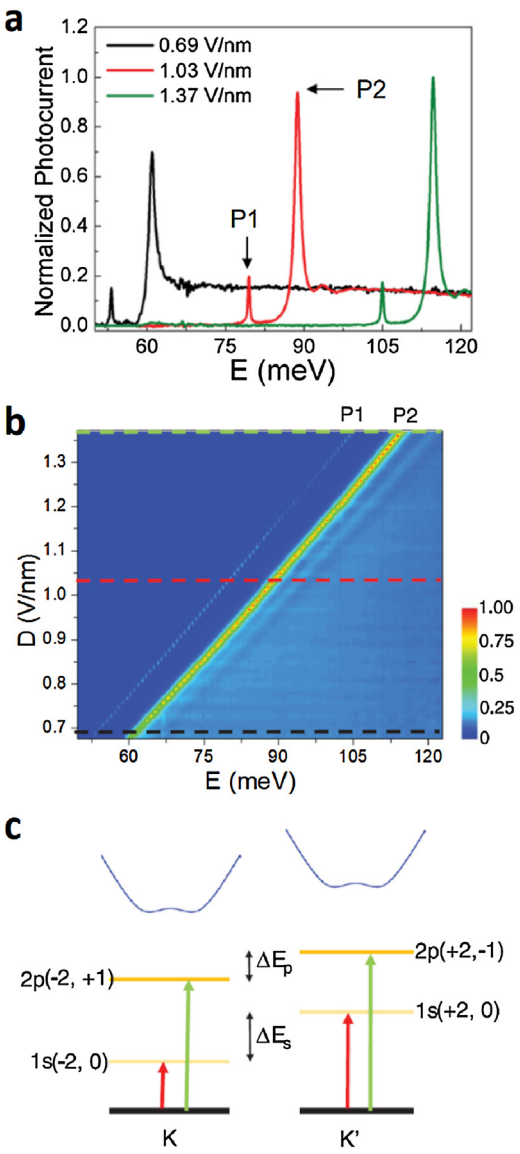

Fig. 4. Electric-field tunable excitons in bilayer graphene. (a) Normalized photocurrent as a function of photon energy in dual-gated bilayer graphene transistor. The two peaks correspond to the two excitons in gapped bilayer graphene. For different vertical displacement fields, the photocurrent peaks are distinctively different, indicating the tuning of excitons. Reproduced with permission [66]. Copyright, 2017, American Association for the Advancement of Science. (b) 2D mapping of photocurrent as function of displacement field *D* and photo energy *E*. Reproduced with permission [66]. Copyright, 2017, American Association for the Advancement of Science. (c) Valley-dependent selection rules and exciton states in gapped bilayer graphene. Arrows denote the optical transitions from ground states (black line) to 1*s* and 2*p* states. Reproduced with permission [66]. Copyright, 2017, American Association for the Advancement of Science.

BP [111]. In monolayer BP, the bandgap size is ~2 eV and its value decreases to ~0.3 eV in bulk, which has been determined by various techniques, including photoluminescence [101,102,120], transport [121], scanning tunneling microscopy (STM) [122] and capacitance [123] (see Fig. 5b). Taking advantage of the desirable direct bandgap of BP, various photodetectors and modulators in both visible and infrared regime are demonstrated [118,119,124–130]. For electronic applications, thin-film BP exhibits high intrinsic carrier mobility up to 5200 $cm^2V^{-1}s^{-1}$ and current on-off ratio over 10^3 at room temperature [112,116,131,132], making it a promising material for radio frequency transistors and logic circuits [133,134]. The detailed electronic and optical properties of BP have been summarized in several reviews [8,9,135–138]. Here, we mainly focused on the electrically tunable physical properties of thin-film BP and associated applications.

Electric field-tunable electronic properties

In 2014, several research works [139–142] predicted that an external electric field along the out-of-lattice-plane direction could effectively tune the bandgap size of thin-film BP (for layer number larger than 1). Different from the electric field-induced bandgap opening in bilayer graphene, the bandgap size of thin-film BP decreases under electric fields. Kim et al. directly observed the widely tunable bandgap of few-layer BP using ARPES (see Fig. 5c) [143]. The electric field is induced at BP surface through deposition of potassium atoms. As shown in Fig. 5d, at a dopant density of 8.3×10^{13} cm^{-2} (0.36 monolayers), the bandgap closes and BP transits from a semiconductor to a Dirac semimetal.

A more flexible and reversible approach to induce the electric field across BP is through the dual-gate structure, similar to the dual-gate bilayer graphene transistor discussed in previous section. In 2017, Deng et al. introduced the dual-gate thin-film BP FET (Fig. 5e) and investigated the bandgap tuning effect using 4-terminal transport measurements [144]. The bandgap size was extracted through fitting the temperature-dependent conductance at charge-neutrality point inside the gap where the thermal excitation of carriers dominates. For a 10 nm-thick BP film, the bandgap can be widely tuned from ~300 meV to below 50 meV at a displacement field of 1.1 V nm^{-1} (see Fig. 5f). The results agree quite well with tight-binding model including the carrier screening effect. For thinner samples, the gap tuning efficiency decreases as a result of smaller voltage drop across BP. Similar bandgap tuning effect in few-layer BP was also observed by Liu et al. using STM (Fig. 5g, h) [145], by Yan et al. using 2-terminal transport [146] and by Chen et al. using photocurrent measurement [119].

Gate-tunable optical properties and applications in optoelectronics

The optical properties of thin-film BP can also be widely tuned under the perpendicular electric fields [119,129,130,147]. Whitney et al. [129] and Peng et al. [130] experimentally studied the optical absorption properties of few-layer BP at different gate biases based on a single-gate structure (Fig. 6a). As shown in Fig. 6b, a maximum optical modulation of 3% is achieved at gate biases of ±150 V in a 9 nm- thick BP sample (on a 450 nm-SiO_2/Si substrate) [130], revealing BP a promising material for mid-infrared electro-optical modulators. The modulation strength and direction strongly depends on the gate bias, as a result of competition between quantum-confined Franz-Keldysh (QCFK) effect and Burstein-Moss (BM) effect [129,130,147]. When an electric field presents in a quantum-confined system, electron and hole wave functions in conductance and valence bands are modulated and will leak into the band gap leading to a redshift of absorption edge (see Fig. 6c). This is called the QCFK effect. On the other hand, gate biases induce doping in BP and shift its Fermi energy. At sufficient large gate biases, Pauli blocking will occur and shift the absorption edge to higher energy resulting in the BM effect.

Compared with the single-gate electro-optical modulation structure, the dual-gate geometry offers another degree of freedom to control the electric field and carrier density in few-layer BP simultaneously. Chen et al. demonstrated a widely tunable BP mid-infrared photodetector based on the dual-gate interdigitated FET structure as shown in Fig. 6d [119]. The 10-layer BP was sandwiched by hBN flakes in an argon-filled glovebox to preserve its high intrinsic quality. The interdigitated structure was used to maximize the photocurrent collection efficiency. By tuning the back gate and top gate biases, a vertical electric field is

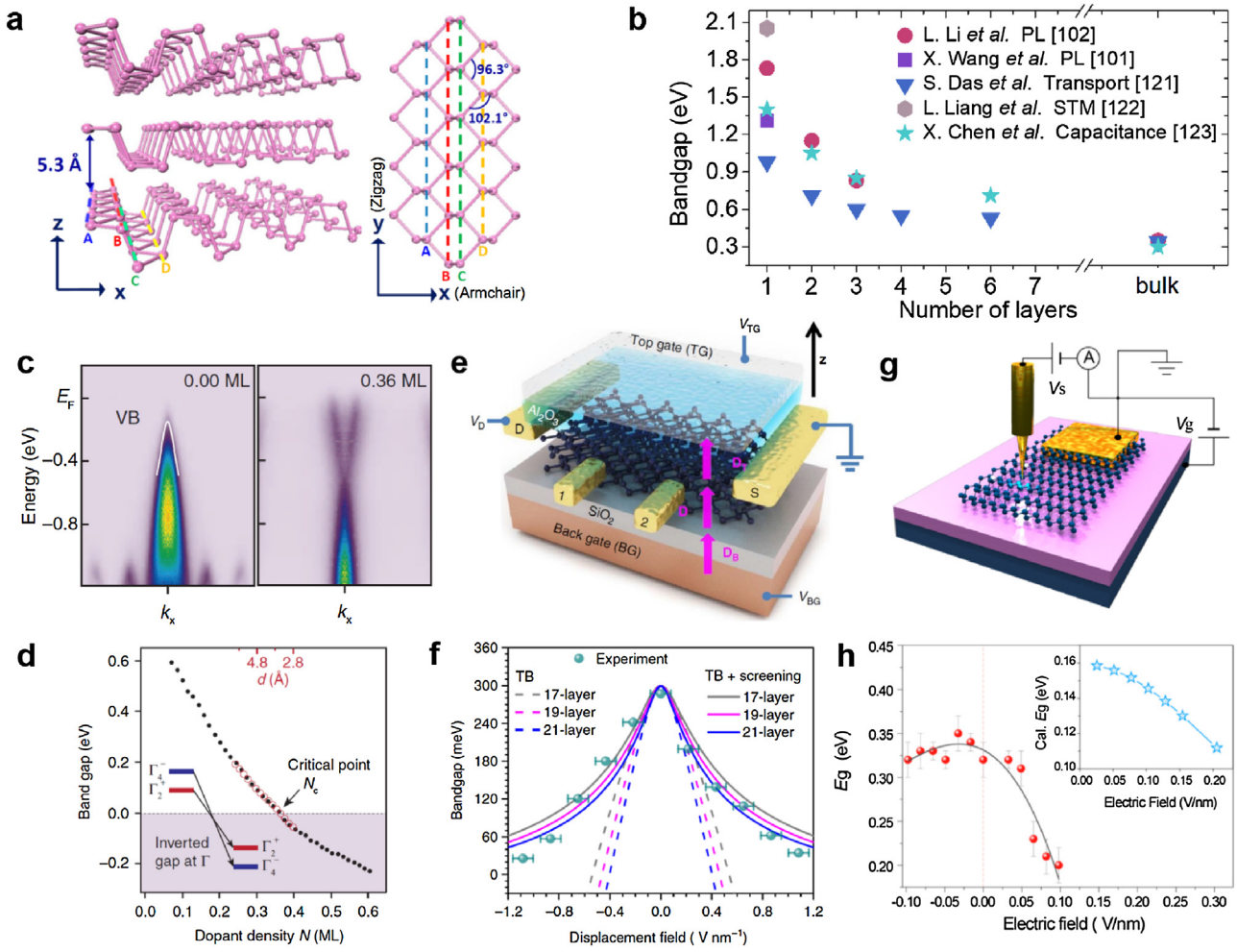

Fig. 5. Electric-field tunable bandgap in thin-film BP. (a) Perspective side view and top view of BP lattice. Reproduced with permission [8]. Copyright, 2015, Proceedings of the National Academy of Sciences of the United States of America. (b) Layer-dependent bandgap of BP detected through various experimental techniques. (c) Band structure of BP without (left panel) and with (right panel) surface potassium doping obtained by ARPES. At a doping density of 0.36 monolayer, the bandgap of BP closes. Reproduced with permission [143]. Copyright, 2015, American Association for the Advancement of Science. (d) Bandgap of BP as a function of dopant density. Black dots denote the experimental results and the red circles denote the DFT calculation results. Reproduced with permission [143]. Copyright, 2015, American Association for the Advancement of Science. (e) Schematic of dual-gate thin-film BP transistors for bandgap tuning. Electric displacement field D is controlled through tuning top and back gate biases. Reproduced with permission [144]. Copyright, 2017, Nature Publishing Group. (f) Bandgap of a 10 nm-thick (19-layer) BP film as a function of displacement field. Green dots are experimental results obtained from temperature-dependent transport at charge-neutrality point. Solid and dashed lines denote the tight-binding calculations with and without taking into account the dynamic screening effect. Reproduced with permission [144]. Copyright, 2017, Nature Publishing Group. (g) Schematic of STM investigation on the bandgap tuning effect of thin-film BP. Reproduced with permission [145]. Copyright, 2017, American Chemical Society. (h) Bandgap of a 11-layer thick BP film as a function of electric field probed by STM. Reproduced with permission [145]. Copyright, 2017, American Chemical Society.

induced across the BP film. At the same time the charge-neutrality point of BP can be accessed, where the BM effect is negligible. For a 10-layer BP film, the intrinsic photoresponse cutoff wavelength is around 4 μm. However, the BP photo-transistor exhibits a significant photocurrent at charge-neutrality point at strong vertical displacement fields ($D > 1\ V\ nm^{-1}$) even under 5 and 7.7 μm mid-infrared light (see Fig. 6e), indicating that the photoresponse cutoff wavelength shifts to longer wavelength [119]. The strong modulation of bandgap and photoresponse through external electric field makes BP a promising material for mid-infrared photodetectors, modulators and spectrometers.

Transition-metal dichalcogenides

Electric field-induced structural phase transition and device applications

Transition-metal dichalcogenides (TMDs) are referred to the layered van der Waals crystals with a chemical structure of MX_2, where M represents the transition-metals such as Mo, W, Nb, Ta, etc., and X represents S, Se and Te [3,4,148]. TMDs have rich structural phases. The most common structural phases in TMDs are the 2H, 1 T and 1 T' phases, as shown in Fig. 7a. TMDs stable in 2H phase (such as MoS_2, $MoSe_2$, $MoTe_2$, WS_2 and WSe_2) are semiconductors, while TMDs stable in 1 T (TaS_2) and 1 T' (WTe_2) phases usually show metallic behavior [148]. The realization of dynamic control of transitions between structural phases can be important in both understanding the interplay of physical properties between phases and achieving novel functional electronic devices.

Several approaches have been investigated to induce 2H to 1 T'/1 T phase transitions in TMDs, such as thermal synthesis at high temperature [149], laser irradiation [150], organolithium intercalation [151], and plasma treatment [152]. However, the phase transitions induced by these methods are irreversible. In 2017, Wang et al. reported a reversible 2H to 1 T' phase transition in monolayer $MoTe_2$ through ion liquid (DEME-TFSI) gating (see inset of Fig. 7b) [153]. At a positive threshold gate voltage ~ 3 V (with an

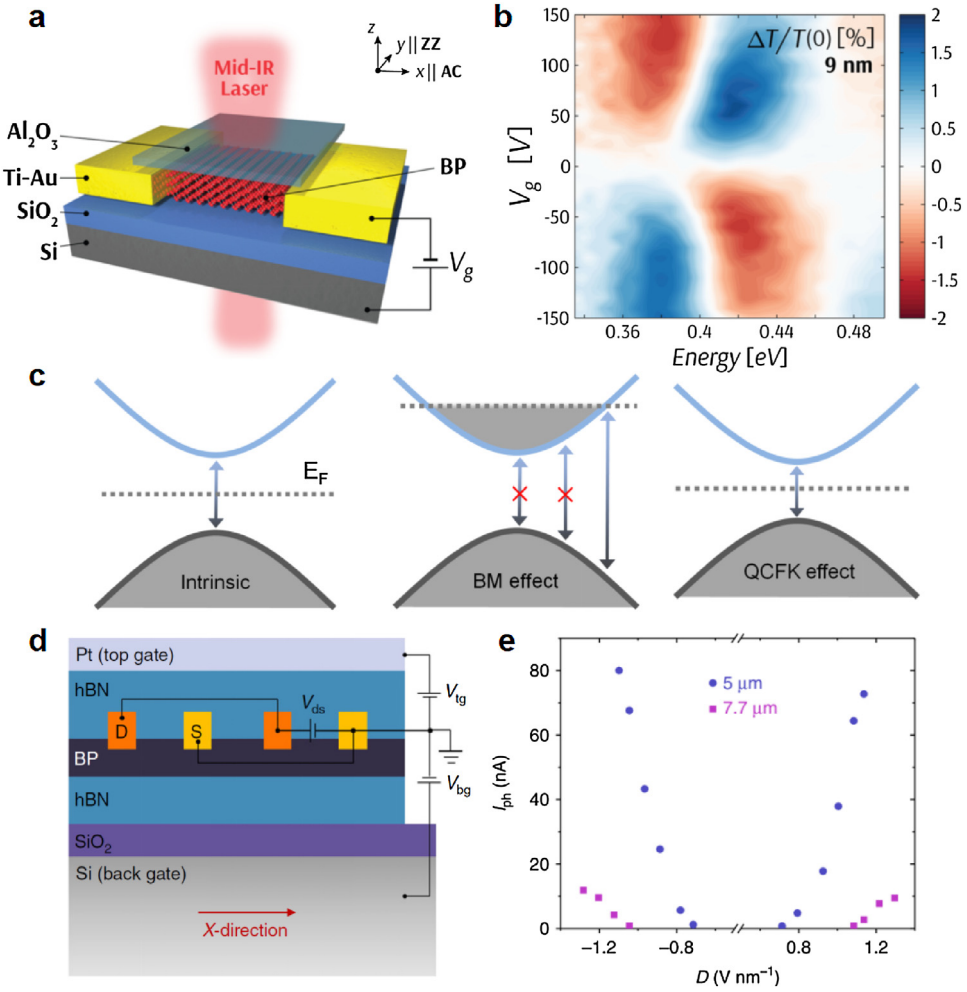

Fig. 6. Gate tunable optical properties of thin-film BP. (a) Schematic of the single-gate thin-film BP transistor for mid-infrared optical absorption measurement. Reproduced with permission [130]. Copyright, 2017, American Chemical Society. (b) Transmission modulation level of a 9 nm-thick BP film as function of energy and gate bias. Reproduced with permission [130]. Copyright, 2017, American Chemical Society. (c) The energy band diagrams of semiconductors under different doping levels. Left panel shows the intrinsic energy band; mid-panel denotes the energy band at the high doping level, where Burstein-Moss (BM) effect dominates as a result of the Pauli blocking; Right panel denotes the influence of quantum-confined Franz-Keldysh (QCFK) effect to the energy band. (d) Schematic of cross-section of the dual-gate interdigitated BP transistor for mid-infrared photodetection. The electric field across BP is controlled through the silicon back gate and thin-film Pt top gate. Reproduced with permission [119]. Copyright, 2017, Nature Publishing Group. (e) Photocurrent as a function of electric displacement field at charge-neutrality point in a 10-layer BP transistor under 5.5 and 7 μm excitation light. Reproduced with permission [119]. Copyright, 2017, Nature Publishing Group.

electron doping ~ 2.2×10^{14} cm^{-2}), the transition from 2H to 1 T' phase occurs, determined by both the Raman characterization of phonon features and second-harmonic generation (SHG) characterization of lattice symmetry [153]. As shown in Fig. 7b, the SHG intensity shows abrupt decrease when gate voltage is increasing from 2 V to 4 V, indicating that the lattice inversion symmetry is recovered at high gate voltage [153]. The observation agrees with the lattice symmetry of $MoTe_2$ in 2H (with broken inversion symmetry) and 1 T' phase (where inversion symmetry is preserved and SHG is prohibited). When lowering gate voltage back to zero, the 2H phase of $MoTe_2$ is recovered without introducing defects in lattice [153].

The capability to induce reversible phase transitions in monolayer $MoTe_2$ through electrostatic doping can be attributed to the small energy difference ~43 meV between 2H and 1 T' phase as shown in Table 2 [154]. Among all Mo- and W- based TMDs, monolayer $MoTe_2$ has the lowest energy barrier between 2H and 1 T' phase, one order smaller than that of other materials listed in Table 2 (except for WTe_2) [154]. Hence, $MoTe_2$ is the best candidate for investigating the dynamic control of phase transitions through electrical gating.

1 T-TaS_2 is another representative TMD that exhibits electrically tunable complex structural phase transitions [155–157]. It exhibits several charge-density-wave (CDW) phases as function of temperature [155–158], pressure [158], electrostatic doping [155], and in-plane electric field [156,157]. Here, CDW describes a macroscopic quantum phenomenon of periodically distortion of the crystal lattice and redistribution of electronic charge densities under external environmental change. Yu et al. reported a tunable CDW phases transitions in thin-film TaS_2 (3.5–23 nm) FET using a gate-controlled lithium (Li) intercalation [155]. In bulk TaS_2 samples (>10 nm), TaS_2 flakes can experience several CDW phase transitions as function of temperature and electrostatic doping, such as the metallic incommensurate CDW (ICCDW) phase, the textured nearly commensurate CDW (NCCDW) phase, and the commensurate CDW phase (CCDW) [155]. However, in 2D limit with flake thickness ~3.5 nm as shown in Fig. 7c, TaS_2 only goes transitions between ICCDW (at high temperatures and doping densities) and NCCDW phases [155]. TaS_2 also exhibits an insulating state which is absent in bulk samples, probably due to the disorders which have a stronger influence on the transport of thinner samples.

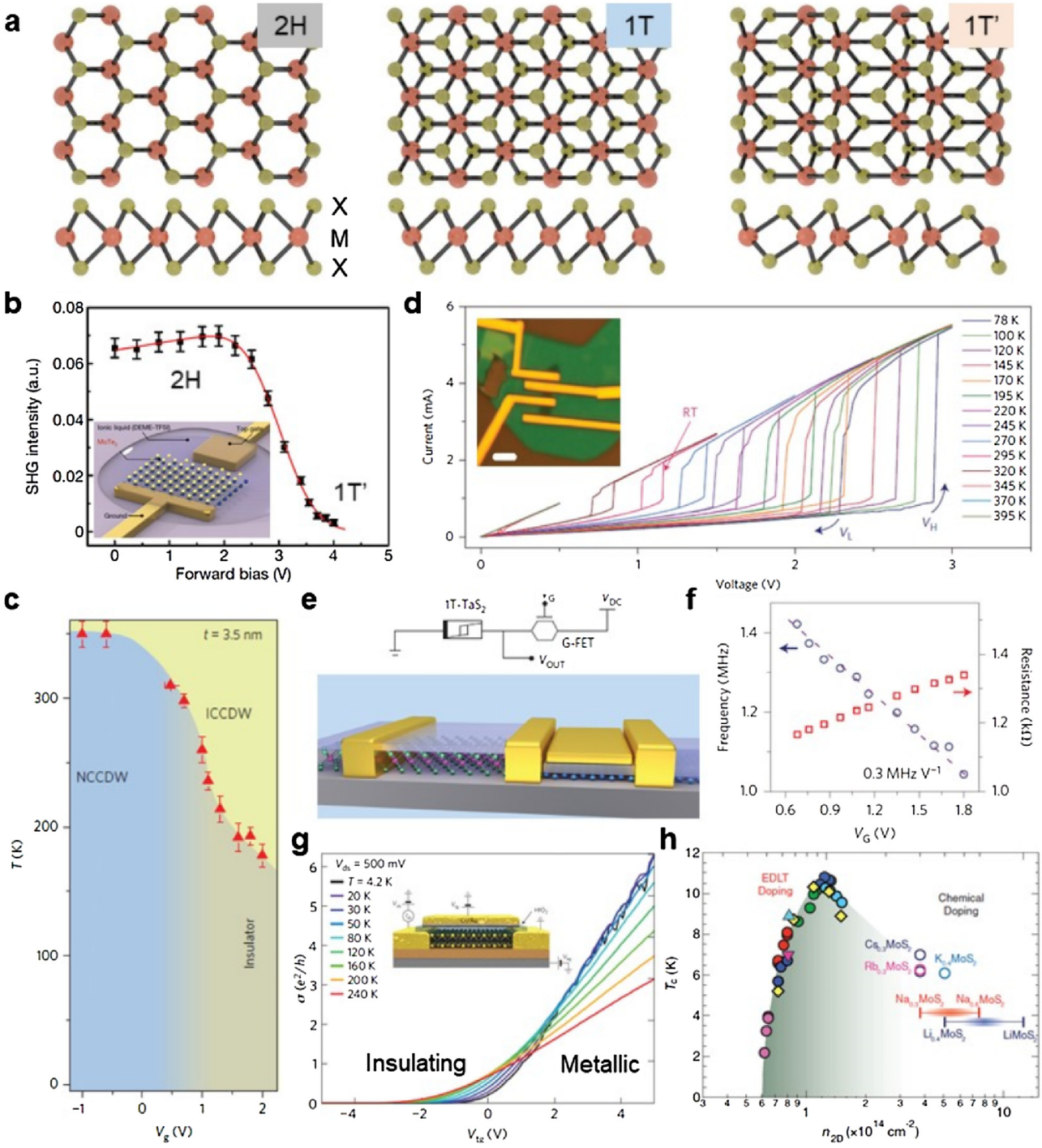

Fig. 7. Electric-field induced structural and transport phase transitions in TMDs. (a) Top and side views of the schematic crystalline structure of TMDs in 2H (left panel), 1 T (mid-panel) and 1 T' (right panel) phases. (b) The second-harmonic generation (SHG) characterization of monolayer $MoTe_2$ under different gate biases. Inset shows the schematic of an ion liquid gated monolayer $MoTe_2$ flake for investigating structural phase transitions. Reproduced with permission [153]. Copyright, 2017, Nature Publishing Group. (c) The charge-density-wave (CDW) phase diagrams as function of temperature T and gate biases V_g in a 3.5 nm-thick 1 T-TaS_2 flake. Reproduced with permission [155]. Copyright, 2015, Nature Publishing Group. (d) In-plane voltage induced CDW phase transitions in a 10 nm-thick TaS_2 flake at various temperatures. Inset shows the optical image of a TaS_2 device. Reproduced with permission [157]. Copyright, 2016, Nature Publishing Group. (e) Schematic of a MHz-frequency oscillator by connecting the TaS_2 transistor with a resistance-tunable graphene transistor. Reproduced with permission [157]. Copyright, 2016, Nature Publishing Group. (f) The gate-tunable oscillation frequency of the TaS_2-graphene oscillator. Reproduced with permission [157]. Copyright, 2016, Nature Publishing Group. (g) The conductivity of the monolayer MoS_2 as a function of gate voltage. The monolayer MoS_2 shows a transport metal-insulator transition. Reproduced with permission [159]. Copyright, 2013, Nature Publishing Group. (h) At higher carrier densities, thin-film MoS_2 shows superconducting behavior below the transition temperature. The transition temperature as a function of gate-induced carrier density in MoS_2 shows a dome-like feature. Reproduced with permission [49]. Copyright, 2012, American Association for the Advancement of Science.

Hollander et al. [156] and Liu et al. [157] showed that a moderate in-plane source-drain voltage could also efficiently induce the NCCDW to ICCDW phase transitions in thin-film TaS_2 ($\tilde{1}$0 nm), as shown in Fig. 7d. At high driven voltages thin-film TaS_2 exhibits the metallic ICCDW phase, while at low voltages it switches back to the high-resistance NCCDW phase. This transition even persists above the room temperature. Taking advantage of this switchable phase transitions of thin-film TaS_2, Liu et al. demonstrated a MHz-

Table 2
Ground phase and energy of 2H, 1 T and 1 T' phase of Mo- and W- based monolayer TMDs. The energy of 2H phase is set to be zero [154].

Phase	MoS_2	$MoSe_2$	$MoTe_2$	WS_2	WSe_2	WTe_2
Ground phase	2H	2H	2H	2H	2H	1 T'
2H (meV)	0	0	0	0	0	86
1 T' (meV)	540	330	43	530	270	0
1 T (meV)	830	690	510	880	760	636

frequency oscillator operating at room temperature [157]. This is realized by connecting the thin-film TaS_2 transistor to a monolayer graphene FET which acts as a resistance-tunable load resistor as shown in Fig. 7e. When the supply voltage V_{DC} is large enough and voltage across TaS_2 channel reaches the forward transition threshold voltage V_H, the resistance of TaS_2 will decrease sharply. In return the voltage across the load resistor (graphene FET) will increase and the voltage across TaS_2 decreases. When the voltage across TaS_2 is below the backward transition threshold voltage V_L, the resistance of TaS_2 will increase instantaneously, and thus form an oscillation loop. Here the graphene FET (load resistor) is to provide a negative feedback to the TaS_2 transistor. Besides, the resistance of graphene FET is gate tunable, which can be utilized to tune the oscillation frequency of the circuit [157]. As shown in Fig. 7f, the tuning sensitivity is around 0.3 MHz V^{-1} [157].

Gate-induced transport phase transition without structural distortion

Under structural phase transitions, the electronic transport properties, such as conductance, also show abrupt changes as discussed in previous section. On the other hand, transport phase transitions can occur as result of the collective behavior of electrons, such as electron-electron interactions and electron-disorder interactions, without introducing any structural distortion. In 2013, Radisavljevic and Kis reported a transport metal-insulator transition (MIT) in monolayer MoS_2 transistors as shown in Fig. 7g [159]. The MoS_2 transistor shows an insulating behavior at low carrier densities (small gate voltage for n-type MoS_2), where the conductivity σ increases when temperature increases. In contrast, the conductivity decreases when temperature increases at high carrier densities, indicating a metallic behavior [159,160]. This MIT phenomenon has also been observed in monolayer and few-layer MoS_2 through capacitance spectroscopy [44]. Other 2D materials, such as WSe_2 [161,162], ReS_2 [163] and BP [164], also show similar gate-dependent transport behavior.

The MIT is an important phenomenon in 2D electron/hole gas systems, including traditional semiconducting system, such as silicon [165,166] and AlGaAs/GaAs heterostructures [167,168]. A high-performance transistor relies on MIT to switch on (metallic state with high current) and off (insulating state with low current). Currently, there are two major theories for MIT in two dimensions [169]. One theory is based on the percolation transition theory [44,166–168,170,171], describing the percolation transport of charge carriers in disordered landscapes, in analogy to the water percolation through soil. The other explanation originates from the strong electron-electron and electron-disorder interaction induced transitions between conducting and localization regimes [159,163,172,173]. Further studies are necessary to clarify the transition mechanisms and the interplay between percolation and quantum phase transition models.

At higher carrier densities ($> 6 \times 10^{13}$ cm^{-2}) achieved through ion liquid gating, few-layer (including monolayer) MoS_2 becomes superconducting below the transition temperature T_c [49,174–177]. As shown in Fig. 7h, T_c as function of carrier density exhibits a dome-shape superconductivity in MoS_2. Recent works further show that gated MoS_2 is an Ising superconductor due to the strong spin-orbit interaction which locks spins to the out-of-plane direction [174–176]. Similar as 2H-MoS_2, other TMDs such as 2H-WS_2 [178–180] and 2H-$MoSe_2$ [180] also exhibit gate-induced metal-superconductor transitions.

Gate-tunable valley properties

The manipulation of valley degrees of freedom attracts great interests in 2D materials beyond graphene [13]. Monolayer TMDs in 2H phase, such as MoS_2, possesses an inversion asymmetric staggered honeycomb lattice (see Fig. 7a), resulting in a non-vanishing Berry curvature with same amplitude but opposite signs in K and K' valleys (Fig. 8a) [181]. Hence, TMDs are believed to be an ideal platform for constructing valleytronic devices.

In 2012, the control of valley polarization through optical helicity was achieved in monolayer MoS_2 [74–76]. Under excitation of left (right) circularly polarized light, carriers in K (K') valley are excited. Then by applying an in-plane electric field between source and drain electrodes, the carriers will curve to the perpendicular direction of electric field while moving, subject to the Berry curvature. In this case, Hall voltage from pure valley current can be directly measured, and it was demonstrated in monolayer MoS_2 transistor as shown in Fig. 8b [181]. The experiment shows a gate-dependent valley Hall current under 1.9 eV circularly polarized light excitation, of which the value increases with carrier densities, while the theory predicts a gate-independent feature (see Fig. 8c). Although several possible scenarios have been taken into account to explain the discrepancy between theory and experiment, such as photoconduction mechanisms and finite contribution from skew-scattering processes [182], more studies are needed to better understand this phenomenon.

Similar to the case of bilayer graphene, an out-of-plane electric field can also break the lattice inversion symmetry of bilayer MoS_2 and thereby control the magnitude of Berry curvatures in K and K' valleys. In 2016, Lee et al. reported the electrically control of the valley polarization in bilayer MoS_2 using an optical Kerr rotation microscopy [183]. With the presence of the electric field (gate voltage), a pronounced valley polarization was observed near the two edges of MoS_2 channels but with opposite signs. The strength and sign of the valley polarization could be further tuned through the gate voltage as shown in Fig. 8d [183].

The generation and detection of valley current in TMDs through purely electrical approach has been a long-standing challenge due to the relatively low carrier mobility compared with that in graphene. Only till recently, Wu et al. and Hung et al. successfully detected the valley current in monolayer MoS_2 through the non-local transport approach [184,185]. By tuning the carrier density of MoS_2 beyond a critical value using gate voltages, a pronounced non-local resistance is observed scaling cubically with the local resistance [184]. The non-local signal can persist at room temperature with a valley diffusion length up to 16 μm [184], suggesting monolayer MoS_2 a promising material for realizing room-temperature low-dissipation valleytronics.

Electrically tunable transport and ferroelectric properties in WTe_2

As a semi-metallic member (with 1 T' as ground phase) in TMDs family, WTe_2 has attracted enormous interest since the bulk crystals were discovered to possess a huge non-saturating magnetoresistance (MR) behavior in 2014 [186]. The nearly perfect electron-hole charge compensation as well as the high carrier mobility are considered as the main source of the extremely large MR observed in WTe_2 [186–193]. In 2015, Wang et al. investigated the magneto-transport of WTe_2 flakes (exfoliated on SiO_2 substrates) at atomic scale and found that the temperature-dependent

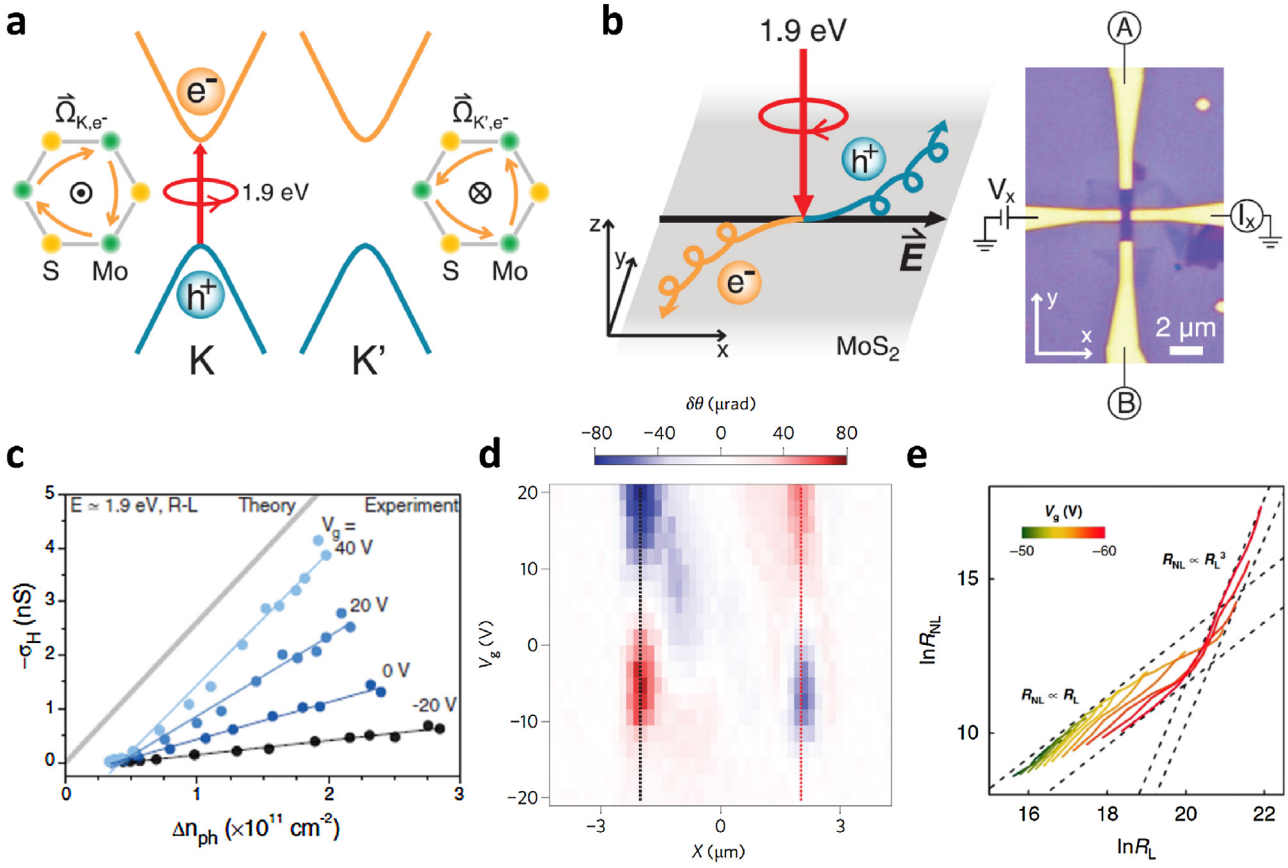

Fig. 8. Gate-tunable valley properties in MoS_2. (a) Band structure and the valley-dependent optical selection rules in monolayer MoS_2. Electrons at the K and K′ valleys possess opposite Berry curvatures $\rightharpoonup \Omega$. Reproduced with permission [181]. Copyright, 2014, American Association for the Advancement of Science. (b) Left panel: schematic of the VHE driven by an in-plane electric field under excitation of the 1.9 eV circular-polarized light. Right panel: optical image of the device for measuring the VHE. Reproduced with permission [181]. Copyright, 2014, American Association for the Advancement of Science. (c) Hall current as a function of the photo-excited carrier density at different gate voltages under the 1.9 eV circular-polarized light. Reproduced with permission [181]. Copyright, 2014, American Association for the Advancement of Science. (d) Kerr rotation mapping as function of gate voltage V_g and position X in bilayer MoS_2. Black dashed line indicates the edge of bilayer MoS_2 flake. Reproduced with permission [183]. Copyright, 2016, Nature Publishing Group. (e) Non-local resistance as a function of local resistance at different temperatures measured in a Hall-bar geometry field-effect transistor. Reproduced with permission [184]. Copyright, 2018, Nature Publishing Group.

transport of WTe_2 films thicker than 5-layer still showed metallic behavior, and more importantly their MR could be well described by the classical two-band model [188]. For 4-layer and thinner flakes, transport shows insulating and weak anti-localization behaviors, due to significant surface scatterings induced by surface degradation in ambient condition [188]. For the same reason, a long-range field effect induced by non-local conductivity was firstly observed in WTe_2 with thickness being much larger than the electrostatic screening length [194]. As shown in Fig. 9a, in a 48nm-thick WTe_2 Hall-bar device, the hall conductance G_{xy} shows dramatic changes (even with signs inverted) with gate voltages which is an unexpected phenomenon in such thick metallic materials [194]. This long-range field effect can be understood as the gate-dependent bulk hole and electron mobilities through charge-tunable surface scatterings. As illustrated in Fig. 9b, when applying a negative gate voltage, holes are attracted towards to surface while electrons are pushed away, resulting in a reduced hole carrier mobility suffering from strong surface scatterings but enhanced electron mobility free of surface scatterings [194]. The electron and the hole mobility of the bulk region vary vastly while their densities keep unchanged [194].

Bulk 1 T'-WTe_2 are also shown to be type-II Weyl semimetals [195], demonstrated by first-principles calculations [196], ARPES [197–199] and magneto-transport measurements [200,201]. When thickness is down to monolayer, 1 T'-WTe_2 is predicted to be a quantum spin Hall insulator exhibiting topological edge states inside the inverted bandgap [202]. Besides, calculations show that the inverted bandgap is over 100 meV, indicating the possible topological transport at a relatively high temperature [203]. However, previous studies before 2017 did not prove such topological effect in monolayer WTe_2 because of the relatively reduced quality after exposure in ambient condition. In 2017, Fei et al. experimentally observed the edge conduction effect in hBN-sandwiched WTe_2 transistors below 100 K [204]. The measured edge conductance is only half of the predicted value of e^2/h, indicating significant inelastic edge scatterings and contact resistance [204]. With further progress in the device quality and measurement strategy, Wu et al. demonstrated the quantum spin Hall effect in monolayer WTe_2 with edge conductance fully quantized to e^2/h (per edge) up to 100 K inside the inverted bandgap (see Fig. 9c) [205]. The quantum spin Hall effect is more robust in short-channel devices at low temperatures, because of reduced edge and phonon scatterings [205]. In addition, because of the weak screening effect in monolayer WTe_2, the competition between bulk states and topological edge states can be conveniently tuned by a gate voltage. Besides transport measurements, STM was also used in studying the band properties and topological edge states of monolayer WTe_2 [206–209]. As the tunneling current is directly proportional to the local density of states, a sharp increase of density of states can be observed near the edge of monolayer WTe_2 [206–209]. Recent transport studies by Fatemi et al. and Sajadi et al. further demonstrate that monolayer WTe_2 becomes a superconductor below 1 K above a mild electron critical

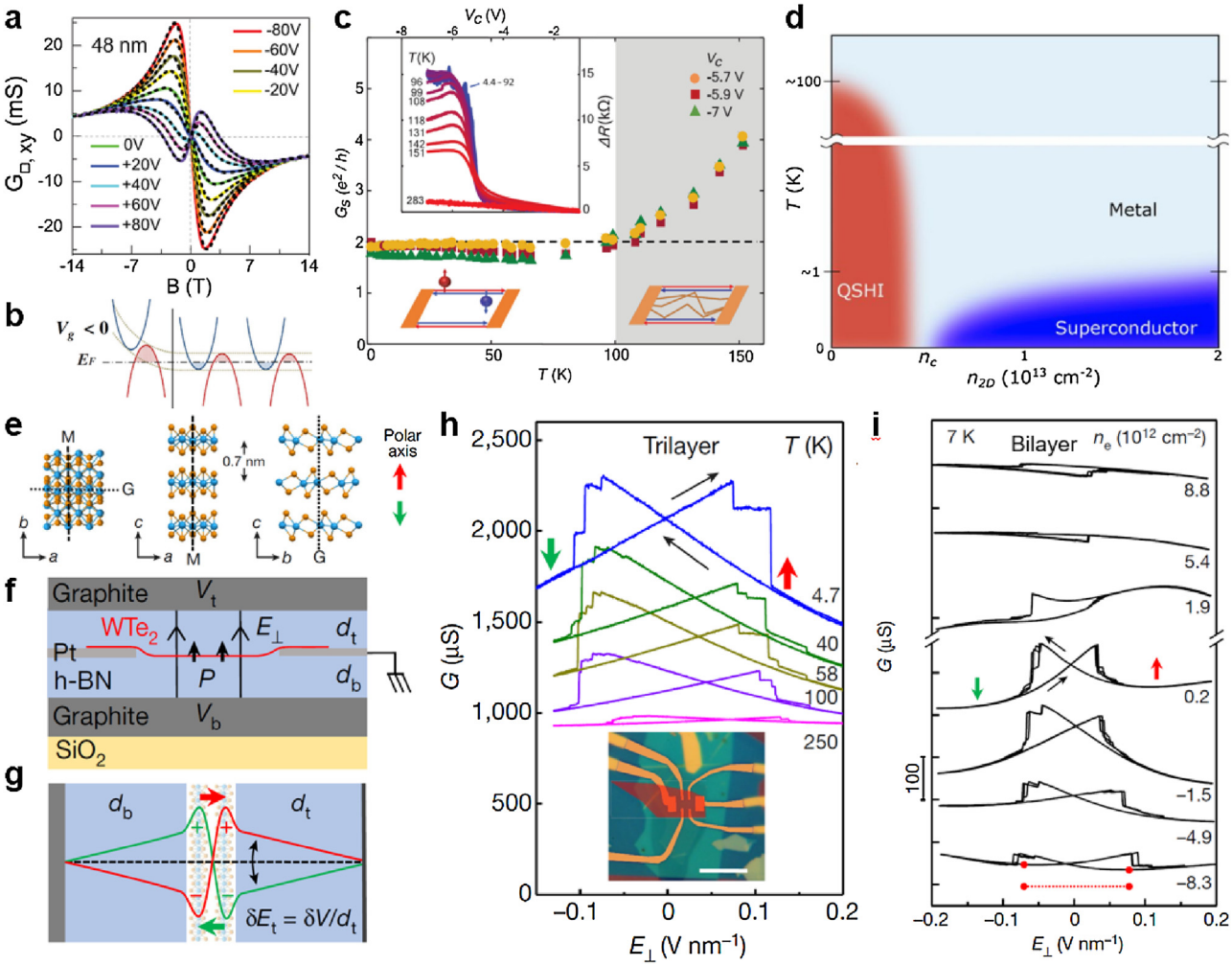

Fig. 9. Electrically tunable transport and ferroelectric properties in 1 T'-WTe_2. (a) Transvers conductance as function of the magnetic field in a 48 nm-thick WTe_2 device for different gate voltages at 250 mK. Reproduced with permission [194]. Copyright, 2016, American Physical Society. (b) Band diagram of multilayer WTe_2 at a negative gate voltage, where electrons are pushed away from surface. Reproduced with permission [194]. Copyright, 2016, American Physical Society. (c) Conductance as function of temperature in monolayer WTe_2. Below 100 K, the conductance is well quantized to the value of $2e^2/h$. Inset shows the conductance as function of gate bias at different temperatures. Reproduced with permission [205]. Copyright, 2018, American Association for the Advancement of Science. (d) Phase diagram of monolayer WTe_2 as function of temperature and carrier densities, showing the temperature- and doping-dependent phase transitions between quantum spin hall insulator, metal and superconductor states. Reproduced with permission [211]. Copyright, 2018, American Association for the Advancement of Science. (e) Schematics of WTe_2 structure. Here M and G represents the mirror plane and glide plane, respectively. Reproduced with permission [212]. Copyright, 2018, Nature Publishing Group. (f) The cross-sectional schematic of the dual-gate WTe_2 device. Reproduced with permission [212]. Copyright, 2018, Nature Publishing Group. (g) Electrostatic potential distribution and the polarization direction (indicated by the red and green arrows) across the device. Reproduced with permission [212]. Copyright, 2018, Nature Publishing Group. (h) Conductance as a function of vertical electric field in trilayer WTe_2 at different temperatures. Inset shows the optical image of the WTe_2 device. Reproduced with permission [212]. Copyright, 2018, Nature Publishing Group. (i) Conductance as a function of vertical electric field in a bilayer WTe_2 at different carrier densities. Reproduced with permission [212]. Copyright, 2018, Nature Publishing Group.

density of 5×10^{12} cm^{-2} (see Fig. 9d) [210,211]. The critical density is only ~0.5% of an electron per W atom, one order smaller than that in 2H-MoS_2 [210,211]. Although the nature of superconductivity in monolayer WTe_2 is still unclear, the ability to switch between the quantum spin hall insulator and superconductor with a local electrostatic gate could open new doors towards realizing Majorana mode in a single material.

Recently, Fei et al. discovered the electrically switching ferroelectric characteristics in bilayer and trilayer WTe_2 [212]. Because the crystal structure of monolayer 1 T'-WTe_2 is centro-symmetric, no ferroelectric switching effect is expected. While for multilayer WTe_2, there exists an electric polar axis along the c-direction due to the b–c mirror symmetry and a–c glide plane (see Fig. 9e) [212]. Bilayer and trilayer WTe_2 flakes are perfect candidates for this ferroelectric switching studies due to the weak screening effect and atomic thickness which allow a perpendicular electric field to efficiently penetrate flakes. To induce the electric field across WTe_2 flakes, the dual-gate structure is adopted as shown in Fig. 9f [212]. Fig. 9h shows the conductance G of a trilayer WTe_2 sample as function of the vertical electric field. The conductance is bistable at electric field $E_\perp = 0$ and the electric polarization (indicated by green and red arrow in Fig. 9h) is switched at a moderate electric field ~ ± 0.1 V nm^{-1} [212]. Moreover, this ferroelectric switching can be sustained to a rather high temperature of 350 K [212]. The polarization-dependent conductance G can be understood as the redistribution of charge carriers and electrostatic potentials (see Fig. 9g) in WTe_2 layers when the electric polarization direction is switched [212]. Hence, the carrier density should also influence the ferroelectric switching properties of WTe_2, as demonstrated by the ferroelectric switching conductance as function of the carrier density shown in Fig. 9i [212]. Those rich electrically tunable physical properties make WTe_2 a very promising candidate in both condensed matter physics studies and novel electronic devices.

Emerging 2D layered magnetic materials

Magnetic order persisting down to monolayer limit is both fundamentally interesting for new quantum phenomenon and engineeringly attractive for novel spintronic devices. According to the Mermin-Wagner theorem [213], the long-range magnetic order is theoretically prohibited in 2D isotropic systems at finite thermal fluctuations. However, recent experiments have demonstrated ferromagnetism and antiferromagnetism in several 2D layered materials down to monolayer limit [214–217], which seems to be contrary to the theoretical predictions [213]. This is because the monolayer and few-layer 2D materials are magnetic anisotropic systems instead of a perfect isotropic 2D Heisenberg system as illustrated in Fig. 10a [214,215]. The magnetic (spin) direction at each site deviates from the out-plane direction and allows the formation of the long-range magnetic order at a finite temperature.

Electrically tunable magnetic properties in CrI_3 and $Cr_2Ge_2Te_6$ – layered semiconducting ferromagnets

The direct magneto-optical Kerr effect (MOKE) measurements on the magnetism in atomically thin layered materials were demonstrated by Huang et al. and Gong et al. in insulating few-layer CrI_3 [214] and $Cr_2Ge_2Te_6$ [215] in 2017, respectively. Different from few-layer $Cr_2Ge_2Te_6$ which shows ferromagnetism at all thickness [215], the magnetic order in CrI_3 is thickness-dependent [214]. Monolayer CrI_3 is a ferromagnet with an out-of-plane magnetic moment, while bilayer CrI_3 shows a surprising antiferromagnetism with antiparallel magnetization (↑and↓) from two layers (see Fig. 10b) [214]. For trilayer CrI_3, the magnetization in each layer is ↑/↓/↑ or ↓/↑/↓, and thus is ferromagnetic [214]. Utilizing this unique antiferromagnetic coupling in few-layer CrI_3 (> 1-layer), spin-filters with giant tunneling magneto-resistance are demonstrated based on graphene/CrI_3/graphene tunneling vdW heterostructures as shown in the inset of Fig. 10c [218–220]. Here, graphene serves as electron and hole sources. Taking bilayer CrI_3 spin-filter device as an example, the ↑↓ and ↓↑ states at magnetic field $\mu_0 H = 0$ are low current states because of the large tunneling barrier height of carriers with different spins [218]. At a relatively small out-of-plane magnetic field ($\mu_0 H_\perp$) ~0.6 T, an antiferromagnet-ferromagnet transition occurs and bilayer CrI_3 enters high current states ↑↑ and ↓↓. The tunneling magneto-resistance (TMR) in bilayer CrI_3 spin-filter device, defined as $(R_{\uparrow\downarrow} - R_{\uparrow\uparrow})/R_{\uparrow\uparrow}$, can be tuned by a DC bias between two graphene electrodes, which reaches ~310% at V = 300 mV as shown in Fig. 10c [218]. The TMR ~530% is even larger for the in-plane spin-alignment by applying an in-plane magnetic field ($\mu_0 H_\parallel$) [218]. For trilayer and four-layer CrI_3 spin-filter devices, the TMR is as high as 3200% and 19,000%, respectively [218].

Due to the vdW nature and the weak interlayer exchange interaction in CrI_3, it is possible to tune the magnetic order strength and antiferromagnet-ferromagnet transitions through non-magnetic external perturbations, such as electrostatic doping [221,222]. As shown in Fig. 10d, the ferromagnetic hysteresis loop of monolayer CrI_3 can be significantly modified by the electrostatic doping [222]. The electron doping (positive gate) strengthens the magnetic order, while the hole doping (negative gate) weakens the magnetic order [222]. Other magnetic parameters, such as coercive force, saturation magnetization and Curie temperature of monolayer CrI_3, are also significantly tuned [222]. In bilayer CrI_3, the electrostatic doping can even induce the antiferromagnet-ferromagnet transition at a critical electron density of 2.5×10^{13} cm^{-2} as shown in Fig. 10e [221,222]. One qualitative explanation is that the doping could modify the interlayer exchange interaction of bilayer CrI_3, and the antiferromagnet-ferromagnet transition would occur when the interlayer exchange interaction overcomes the demagnetization energy [221,222]. With the presence of an out-of-plane magnetic field, the demagnetization energy is lowered, and hence the transition occurs at a lower electron density [221,222]. Recent first-principles calculations show that the antiferromagnet-ferromagnet transition in bilayer CrI_3 could be attributed to the transition of lattice stacking orders [223]. Two energy minimums of lattice stacking orders are identified in bilayer CrI_3 [223]. The global minimum is referred as AB-stacking with ferromagnetism, and the local minimum (with energy close to the global minimum) is referred as AB'-stacking with antiferromagnetism [223]. Stacking order transitions could occur with the presence of electrostatic doping [223]. Further systematic experimental studies are needed to explore the transition mechanisms.

The electric-field controllable magnetic properties are also observed in few-layer ferromagnetic $Cr_2Ge_2Te_6$ recently [224]. Fig. 10g shows the normalized spin magnetization as a function of gate voltage in a 3.5 nm-thick $Cr_2Ge_2Te_6$ FET [224]. The experimental results (open dots) show an enhanced spin magnetization at both electron and hole doping (< 1×10^{13} cm^{-2}), consistent with the first-principles calculations and micromagnetic simulations (solid dots) [224]. Based on the calculations, the spin magnetization in $Cr_2Ge_2Te_6$ is contributed by the p orbital of Te atoms near the valence band (spin down) and the d orbital of Cr atoms near the conduction band (spin up) [224]. As illustrated in Fig. 10f, hole (electron) doping will deplete (fill) the spin minority (majority) states from p orbital of Te atoms (d orbital of Cr atoms) near the valence (conduction) band and hence results in an enhanced magnetization [224].

Electrically tunable magnetic properties in Fe_3GeTe_2 – a layered metallic ferromagnet

Besides layered semiconducting magnets, 2D layered metallic magnets exhibiting itinerant ferromagnetism, such as Fe_3GeTe_2, are also brought into out sight recently [216,217,225]. In 2018, Deng et al., Fei et al., and Tan et al. reported the itinerant Ising ferromagnetism in atomically thin Fe_3GeTe_2 flakes [216,217,225]. Similar as CrI_3 and $Cr_2Ge_2Te_6$, the intrinsic ferromagnetism of Fe_3GeTe_2 is preserved down to monolayer limit, due to the magnetic anisotropy in vdW layered materials [216,217].

Compared with CrI_3, few-layer Fe_3GeTe_2 has better chemical stability and higher Curie temperature. As shown in Fig. 11a, the Curie temperature in monolayer Fe_3GeTe_2 is ~130 K [216,217], much higher compared with that ~45 K in monolayer CrI_3 [214]. With increasing thickness, the Curie temperature of Fe_3GeTe_2 gradually increases and finally saturates to a value of 205 K in bulk form [216,217]. Through the investigation of the thickness-dependent Curie temperature, the 3D to 2D Ising ferromagnetism transition in Fe_3GeTe_2 is found at a critical thickness of 4 nm (five layers) [217]. Fig. 11b shows the phase diagram of Fe_3GeTe_2 magnetic states as function of temperature and thickness [217]. Above the thickness of 15 nm, Fe_3GeTe_2 flakes exhibit a different ferromagnetic state (FM2) because of the formation of labyrinthine magnetic domains [217]. Magnetic force microscopy (MFM) [217], photo-emission electron microscopy (PEEM) [226] and STM [227] are performed to confirm the origin of FM2 state in thick Fe_3GeTe_2 flakes.

Recently, Deng et al. successfully tuned the magnetic properties of atomically thin Fe_3GeTe_2 flakes through ionic gating effect (see Fig. 11c) [216]. As Fe_3GeTe_2 is a metallic material, its magnetic properties can be directly studied through transport, such as the Hall resistance. Fig. 11d shows the anomalous Hall effect in a trilayer Fe_3GeTe_2 device at different gate voltages [216]. The ferromagnetic hysteresis loops are significantly modified by ionic gating. At ionic gating voltages of 1.75 V, the Curie temperature in trilayer is enhanced from 100 K to room temperature [216]. Calculations based on the anisotropic Heisenberg model show that

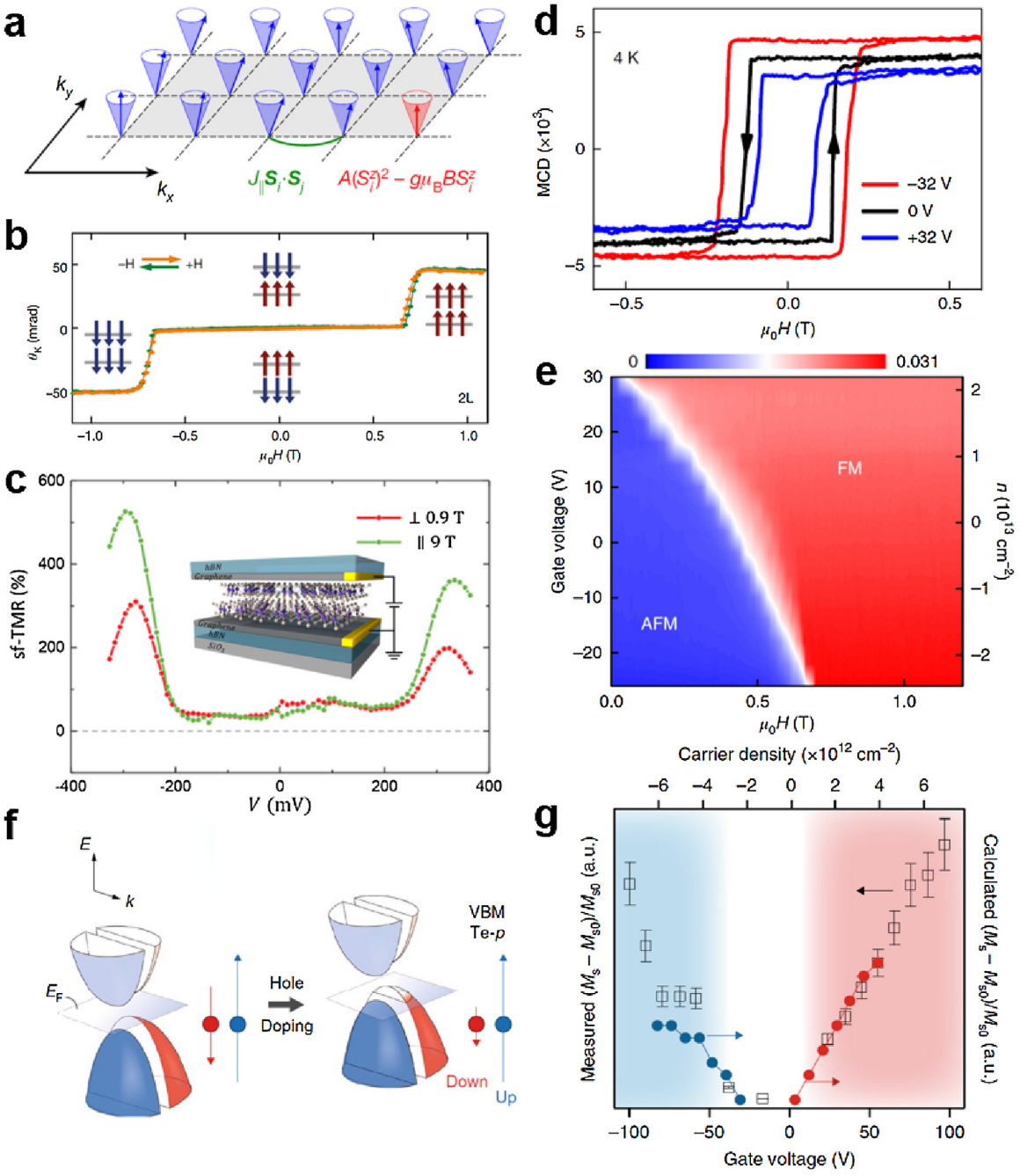

Fig. 10. Electrically tunable magnetic properties of CrI_3 and $Cr_2Ge_2Te_6$. (a) Schematic of the long-range magnetic order in 2D anisotropic magnetic systems. Reproduced with permission [215]. Copyright, 2017, Nature Publishing Group. (b) Magneto-optical Kerr effect (MOKE) in a bilayer CrI_3 sample. Reproduced with permission [214]. Copyright, 2017, Nature Publishing Group. (c) Tunneling magnetic resistance (TMR) as a function of DC excitation bias in the graphene/bilayer-CrI_3/graphene device at vertical (0.9 T) and parallel (9 T) magnetic fields. Inset shows the schematic of graphene/CrI_3/graphene tunneling spin filters. Reproduced with permission [218]. Copyright, 2018, American Association for the Advancement of Science. (d) Magnetic circular dichroism (MCD) signal in a monolayer CrI_3 device for different gate voltages. Reproduced with permission [222]. Copyright, 2018, Nature Publishing Group. (e) MCD signal as function of gate voltage and magnetic field in a bilayer CrI_3 device. Reproduced with permission [222]. Copyright, 2018, Nature Publishing Group. (f) Schematic band diagram of spin alignments at different Fermi energy in $Gr_2Ge_2Te_6$. Red (blue) color represents the spin down (up) contributed from Te (Cr) atoms. Reproduced with permission [224]. Copyright, 2018, Nature Publishing Group. (g) Normalized spin magnetization as function of gate voltages in the 3.5 nm-thick $Gr_2Ge_2Te_6$ device. Black open dots are experimental results and solid blue and red dots are theoretical calculated results. Reproduced with permission [224]. Copyright, 2018, Nature Publishing Group.

electron doping can induce shifting of electronic band of Fe_3GeTe_2 through filling Fe d_{z^2}, d_{xy} and d_{yz} orbitals, cause dramatic changing of density of states at Fermi level and result in the large modulation of its ferromagnetic properties [216].

Utilizing the ferromagnetic properties of thin-film Fe_3GeTe_2, tunneling spin valves based on the Fe_3GeTe_2/hBN/Fe_3GeTe_2 vdW heterostructures are demonstrated (see Fig. 11e) [228]. When the magnetization orientations in two Fe_3GeTe_2 layers (L1 and L2 indicated in Fig. 11e) are parallel (anti-parallel), the tunneling magnetoresistance (TMR) reaches the minimum (maximum) value [228]. This is realized by choosing two different Fe_3GeTe_2 layers with different spin-flip transition fields, which can be monitored by the anomalous Hall effect [228]. By applying a voltage bias between two Fe_3GeTe_2 layers, the TRM is tuned. As shown in Fig. 11f, the

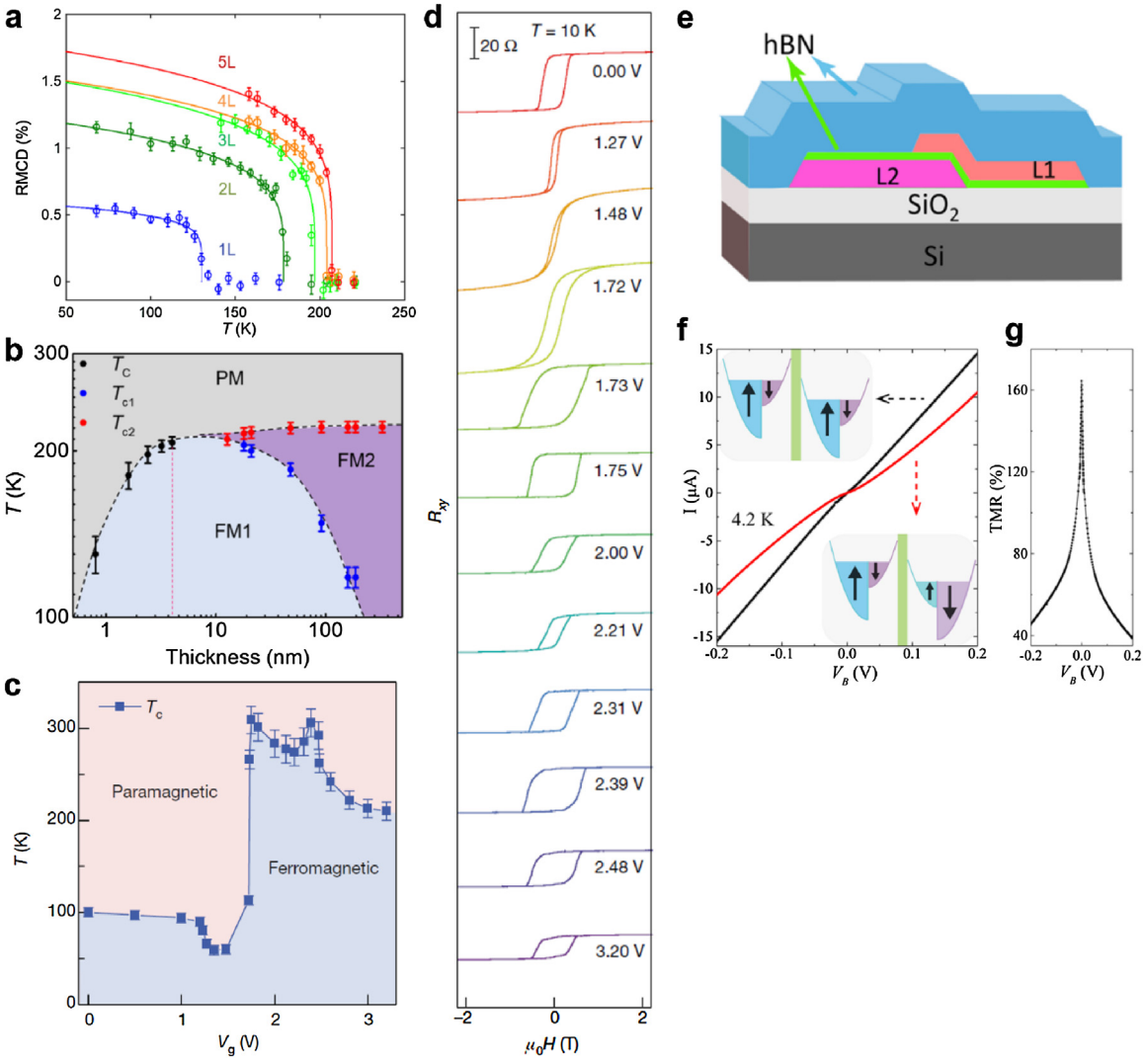

Fig. 11. Magnetic properties of Fe_3GeTe_2. (a) Reflective magnetic circular dichroism (RMCD) signal as a function of temperature in 1–5 layer Fe_3GeTe_2 flakes. Reproduced with permission [217]. Copyright, 2018, Nature Publishing Group. (b) Temperature- and thickness- dependent phase diagram of Fe_3GeTe_2 flakes. Reproduced with permission [217]. Copyright, 2018, Nature Publishing Group. (c) Gate- and temperature- dependent phase diagram of a trilayer Fe_3GeTe_2 sample. Reproduced with permission [216]. Copyright, 2018, Nature Publishing Group. (d) Anomalous Hall resistance R_{xy} as a function of magnetic field at different gate voltages. Reproduced with permission [216]. Copyright, 2018, Nature Publishing Group. (e) Schematic of Fe_3GeTe_2/hBN/Fe_3GeTe_2 tunneling spin valves. Reproduced with permission [228]. Copyright, 2018, American Chemical Society. (f) The tunneling current as a function of voltage bias applied between two Fe_3GeTe_2 layers (L1 and L2) at 4.2 K at magnetic field of 0 T (black line) and -0.68 T (red line), respectively. Reproduced with permission [228]. Copyright, 2018, American Chemical Society. (g) TMR as a function of voltage bias applied between L1 and L2. Reproduced with permission [228]. Copyright, 2018, American Chemical Society.

TMR is suppressed at high bias as a result of the opening of inelastic tunneling pathways and enhanced spin relaxation rates [228].

Other layered magnetic materials

In addition to CrI_3, $Cr_2Ge_2Te_6$, and Fe_3GeTe_2, many other layered magnetic materials have also been investigated using various approaches. For example, Ising-type antiferromagnetic orders in monolayer and few-layer insulating $FePS_3$ with a Neel temperature T_N ~118 K have been observed experimentally using Raman spectroscopy [229]. Theories also predict that metal phosphorous trichalcogenides (including $FePS_3$, $MnPSe_3$, etc.) can experience an antiferromagnetism to ferromagnetism transition at the high carrier doping as shown in Fig. 12a [230,231]. Layered metallic antiferromagnets, such as Ag_2CrO_2, with a Neel temperature (T_N) approaching 24 K, are studied using transport [232,233]. As the paramagnetic scattering of conducting electrons are significantly suppressed near T_N, an abrupt decreasing in longitudinal resistivity (ρ_{xx}) of Ag_2CrO_2 would occur [233]. Apart from Ag_2CrO_2, first-principles calculation also predicts monolayer Mn_2C to be an itinerant antiferromagnets with a crystalline structure similar to that of TMDs in 2H phase [234]. It possesses a high theoretical carrier mobility ~47,000 $cm^2V^{-1}s^{-1}$ and an extremely high Neel temperature of 720 K (see Fig. 12b) [234]. Other ferromagnetic monolayers, such as $MnSe_2$ [235] and VSe_2 [236], have also been demonstrated recently.

Different from previously introduced magnets, $Cr_{1/3}NbS_2$ is a chiral helimagnet with quasi-2D structure [237–240]. As shown in Fig. 12b, the spin makes a complete 2π revolution with a length period of L_0 ~48 nm along the out-of-plane direction of $Cr_{1/3}NbS_2$ [237–240]. This particle like nontrivial magnetic structure is also referred as the magnetic soliton, and the number of solitons in a flake is determined by the thickness and L_B. An external in-plane magnetic field will increase the length of magnetic solitons and hence decrease the number of solitons. When above a critical field, $Cr_{1/3}NbS_2$ becomes a ferromagnet. In 2017, Wang et al. showed

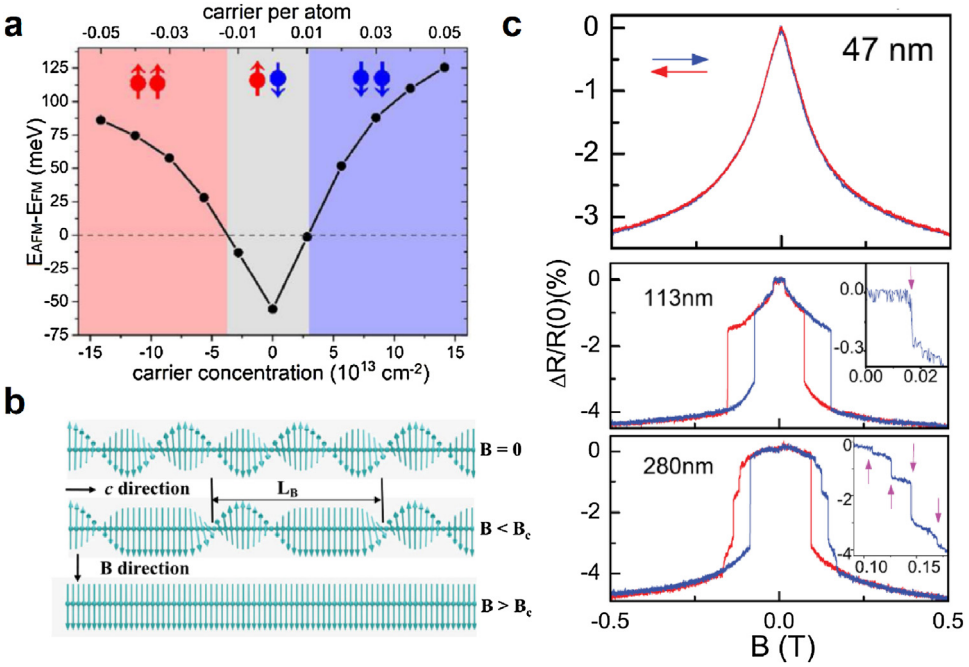

Fig. 12. Magnetic properties of several other layered magnets. (a) Calculated energy difference between antiferromagnetic state and ferromagnetic states of $MnPSe_3$ as a function of carrier concentration. Reproduced with permission [230]. Copyright, 2014, American Chemical Society. (b) Schematic of spin polarization in bulk $Cr_{1/3}NbS_2$. With increasing magnetic field B, the soliton length increases and hence the number of soliton decreases. When above a critical magnetic field B_c, spin polarization will be aligned with the external magnetic field. Reproduced with permission [240]. Copyright, 2017, American Physical Society. (c) Normalized resistance of $Cr_{1/3}NbS_2$ as a function of external magnetic field at various thickness. Reproduced with permission [240]. Copyright, 2017, American Physical Society.

direct evidence that the step-like jumps in the magnetoresistance of $Cr_{1/3}NbS_2$ crystals are related to the deleting/writing of solitons (see Fig. 12c) [240]. When $Cr_{1/3}NbS_2$ thickness is below 48 nm as shown in Fig. 12c, no step-like features are observed because no soliton exists in such systems [240]. The ability to control and detect soliton numbers in $Cr_{1/3}NbS_2$ through magneto-transport shows its promising applications in spintronics.

Major challenges and future look

Although many electrically tunable physical properties of 2D materials are very attractive, a high carrier doping density ($\tilde{1}0^{14}$ cm^{-2}) is required to realize the tuning effect which can be only achieved using ion liquid gating or carrier doping by foreign atoms. Hence these electrically tunable properties cannot be utilized for practical device applications. For example, monolayer $MoTe_2$ shows the 2H (semiconducting) to 1 T' (metallic) phase transition at a doping density of 2.2×10^{14} cm^{-2} tunable by the ion liquid gating, as discussed in previous section [153]. At such a high carrier density, the conductivity of $MoTe_2$ in 2H phase is already very high, and thus the current on-off ratio before and after phase transition should be low. More efforts are still needed for further applications of $MoTe_2$ on phase change devices.

Besides, there are also various 2D layered materials with rich lattice structures and interesting physical properties but less investigated. For example, few-layer InSe flakes show a high electron mobility over 1000 cm^{2}V^{-1}s^{-1} at room temperature [241], monolayer GeS is also theoretically predicted to be a high carrier mobility material [242], In_2Se_3 is a piezoelectric and ferroelectric material [243], and GaS and GaSe flakes show potential applications in optoelectronics [244]. Detailed physical properties and device applications of these 2D metal chalcogenides and trichalcogenides are summarized in Ref. [245]. Moreover, monolayer GeS family (including GeSe, GeS, SnSe and SnS) has been theoretically predicted to exhibit giant piezoelectricity, two orders of magnitude larger than that of traditional bulk piezoelectric materials, such as ZnO and α-quartz, and emerging 2D piezoelectric material, such as monolayer MoS_2 [246]. The electrically tunable piezoelectric properties and related device applications are also expected. More theoretical and experimental efforts are still needed to investigate the electrically tunable physical properties of these 2D materials.

Recently, twisted bilayer graphene system attracts great attention due to the observation of superconductivity at an extraordinary low carrier density of $\tilde{1} \times 10^{12}$ cm^{-2}, which is achievable using the insulated-gate structure [247]. Moreover, Mott-like insulator to superconductor transition can be realized in twisted bilayer graphene system at such a low doping density [247]. Hence, the twisted 2D material system, including twisted bilayer graphene and TMD systems, could provide a new platform for investigating the novel electrically tunable properties and related device applications.

Electron-phonon interactions play an important role in various physical phenomena, including the intrinsic carrier mobility, carrier saturation velocity and formation of Cooper pairs [248]. Through tuning the electron-phonon interactions, the related physical properties of materials and device performance can be controlled. However, electrically tunable electron-phonon interactions are less investigated in 2D material and vdW heterostructure systems. Recently, novel phonon modes were observed in WSe_2/hBN, TMDs/SiO_2, and BP/SiO_2 systems, attributed to the electron-phonon interactions between layered material and substrates [249,250]. Besides, the phonon modes can inherit the band properties of 2D materials, such as valley properties in TMDs. Hence electrical control of electron-phonon interactions in 2D material and vdW heterostructure could offer opportunities in novel valley-electronic and photonic device applications.

Despite the fancy properties of 2D materials, the wafer-scale production of high quality atomically thin 2D materials is still a general challenge for industrial applications with low price and high yield. Up to today, only few 2D materials, such as graphene

and hBN, have been successfully synthesized in wafer-scale single-crystalline structure [251,252]. The wafer-scale synthetic TMDs, including MoS_2 and WS_2, produced thus far are typically polycrystalline [253]. The size of large-scale polycrystalline BP thin films synthesized is limited to 5 mm [254]. Great efforts are needed to improve the material synthetic techniques and develop new synthetic methods.

Nevertheless, 2D materials research is a rapidly growing field, and there are numerous opportunities to achieve novelty and breakthrough. From the perspective of fundamental physics, 2D materials provide a vast and novel platform for investigating electro-matter interactions. Especially, in recently years, more and more 2D materials with rich physical properties are uncovered boosting the further development of this field. As theoretically predicted, there exists thousands of 2D material species which are still not investigated. Moreover, vdW heterostructures with numerous functions can be constructed by assembling different 2D materials layer by layer into vertical stacks, providing new opportunities for studying electro-matter interactions.

From the perspective of engineering, 2D materials are compatible with the traditional silicon-CMOS technology, and can lead to new functional devices utilizing the advantages of both silicon and 2D materials. The 2D material-silicon hybrid technology can also provide a short-cut to the success of industrial applications of 2D materials, before the performance and the cost of all-2D material systems are comparable to those of silicon systems. Taking advantage of the strong electro-matter interaction properties of 2D materials and mature technologies of silicon, on-chip devices, such as electro-optical modulators and tunable electronic circuits, are very promising for commercialization in near future.

Conclusion

In summary, we have provided a comprehensive review of the electrically tunable physical properties of 2D materials. The atomically thin nature of 2D materials favors the strong electro-matter interactions, which enables a widely tunable electronic, optical, and magnetic properties at a mild electric field. Proof-of-concept devices based on the electrically tunable properties, such as dual-gate transistors, valley valves, oscillators, photodetectors, optical modulators and tunneling spin valves, are also introduced in detail.

Competing financial interests

The authors declare no competing financial interest.

Acknowledgements

This work was supported by the Start-up Funding of Southern University of Science and Technology, the National Natural Science Foundation of China (Grant No. 91833302, 61801210), the Natural Science Foundation of Jiangsu Province (Grant No. BK20180686) and the Research Grants Council of Hong Kong (Grant No. 16300717).

References

[1] K.S. Novoselov, A.K. Geim, S.V. Morozov, D. Jiang, Y. Zhang, S.V. Dubonos, et al., Science 306 (2004) 666–669.
[2] A.K. Geim, K.S. Novoselov, Nat. Mater. 6 (2007) 183–191.
[3] K.S. Novoselov, D. Jiang, F. Schedin, T.J. Booth, V.V. Khotkevich, S.V. Morozov, et al., Proc. Natl. Acad. Sci. U. S. A. 102 (2005) 10451–10453.
[4] Q.H. Wang, K. Kalantar-Zadeh, A. Kis, J.N. Coleman, M.S. Strano, Nat. Nanotechnol. 7 (2012) 699–712.
[5] F.H. Koppens, T. Mueller, P. Avouris, A.C. Ferrari, M.S. Vitiello, M. Polini, Nat. Nanotechnol. 9 (2014) 780–793.
[6] C.R. Dean, A.F. Young, I. Meric, C. Lee, L. Wang, S. Sorgenfrei, et al., Nat. Nanotechnol. 5 (2010) 722–726.
[7] L. Song, L.J. Ci, H. Lu, P.B. Sorokin, C.H. Jin, J. Ni, et al., Nano Lett. 10 (2010) 3209–3215.
[8] X. Ling, H. Wang, S.X. Huang, F. Xia, M.S. Dresselhaus, Proc. Natl. Acad. Sci. U. S. A. 112 (2015) 4523–4530.
[9] H. Liu, Y.C. Du, Y.X. Deng, P.D. Ye, Chem. Soc. Rev. 44 (2015) 2732–2743.
[10] N. Mounet, M. Gibertini, P. Schwaller, D. Campi, A. Merkys, A. Marrazzo, et al., Nat. Nanotechnol. 13 (2018) 246–254.
[11] Y. Zhang, Y.W. Tan, H.L. Stormer, P. Kim, Nature 438 (2005) 201–204.
[12] S. Das Sarma, S. Adam, E.H. Hwang, E. Rossi, Rev. Mod. Phys. 83 (2011) 407–470.
[13] J.R. Schaibley, H.Y. Yu, G. Clark, P. Rivera, J.S. Ross, K.L. Seyler, et al., Nat. Rev. Mater. 1 (2016) 16055.
[14] C.L. Kane, E.J. Mele,Phys. Rev. Lett. 95 (2005), 226801.
[15] K.S. Burch, D. Mandrus, J.-G. Park, Nature 563 (2018) 47–52.
[16] A.K. Geim, I.V. Grigorieva, Nature 499 (2013) 419–425.
[17] Y. Liu, N.O. Weiss, X. Duan, H.-C. Cheng, Y. Huang, X. Duan, Nat. Rev. Mater. 1 (2016) 16042.
[18] L. Britnell, R.V. Gorbachev, R. Jalil, B.D. Belle, F. Schedin, A. Mishchenko, et al., Science 335 (2012) 947–950.
[19] W.J. Yu, Z. Li, H.L. Zhou, Y. Chen, Y. Wang, Y. Huang, et al., Nat. Mater. 12 (2013) 246–252.
[20] K.S. Novoselov, A. Mishchenko, A. Carvalho, A.H. Castro Neto, Science 353 (2016), aac9439.
[21] F. Withers, O. Del Pozo-Zamudio, A. Mishchenko, A.P. Rooney, A. Gholinia, K. Watanabe, et al., Nat. Mater. 14 (2015) 301–306.
[22] C. Palacios-Berraquero, M. Barbone, D.M. Kara, X. Chen, I. Goykhman, D. Yoon, et al., Nat. Commun. 7 (2016) 12978.
[23] F. Withers, O. Del Pozo-Zamudio, S. Schwarz, S. Dufferwiel, P.M. Walker, T. Godde, et al., Nano Lett. 15 (2015) 8223–8228.
[24] C.-H. Lee, G.-H. Lee, A.M. van der Zande, W. Chen, Y. Li, M. Han, et al., Nat. Nanotechnol. 9 (2014) 676.
[25] Y. Deng, Z. Luo, N.J. Conrad, H. Liu, Y. Gong, S. Najmaei, et al., ACS Nano 8 (2014) 8292–8299.
[26] W.J. Yu, Y. Liu, H.L. Zhou, A.X. Yin, Z. Li, Y. Huang, et al., Nat. Nanotechnol. 8 (2013) 952–958.
[27] K. Roy, M. Padmanabhan, S. Goswami, T.P. Sai, G. Ramalingam, S. Raghavan, et al., Nat. Nanotechnol. 8 (2013) 826.
[28] D. Li, M. Chen, Z. Sun, P. Yu, Z. Liu, P.M. Ajayan, et al., Nat. Nanotechnol. 12 (2017) 901.
[29] C. Liu, X. Yan, X. Song, S. Ding, D.W. Zhang, P. Zhou, Nat. Nanotechnol. 13 (2018) 404–410.
[30] A.H. Castro Neto, F. Guinea, N.M.R. Peres, K.S. Novoselov, A.K. Geim, Rev. Mod. Phys. 81 (2009) 109–162.
[31] W. Zhao, R.M. Ribeiro, M. Toh, A. Carvalho, C. Kloc, A.H. Castro Neto, et al., Nano Lett. 13 (2013) 5627–5634.
[32] S. Deng, A.V. Sumant, V. Berry, Nano Today 22 (2018) 14–35.
[33] N. Levy, S.A. Burke, K.L. Meaker, M. Panlasigui, A. Zettl, F. Guinea, et al., Science 329 (2010) 544–547.
[34] F. Guinea, M.I. Katsnelson, A.K. Geim, Nat. Phys. 6 (2010) 30–33.
[35] Y.P. Liu, J.N.B. Rodrigues, Y.Z. Luo, L.J. Li, A. Carvalho, M. Yang, et al., Nat. Nanotechnol. 13 (2018) 828.
[36] H.J. Conley, B. Wang, J.I. Ziegler, R.F. Haglund, S.T. Pantelides, K.I. Bolotin, Nano Lett. 13 (2013) 3626–3630.
[37] A.S. Rodin, A. Carvalho, A.H. Castro Neto,Phys. Rev. Lett. 112 (2014), 176801.
[38] S. Song, D.H. Keum, S. Cho, D. Perello, Y. Kim, Y.H. Lee, Nano Lett. 16 (2016) 188–193.
[39] S.M. Sze, K.K. Ng, Physics of Semiconductor Devices, 2nd ed., Wiley, New York, 1981.
[40] T. Ando, A.B. Fowler, F. Stern, Rev. Mod. Phys. 54 (1982) 437–672.
[41] D. Kahng, Electric field controlled semiconductor device, US Patent 3, 102, 230, 1963.
[42] S.L. Chuang, Physics of Photonic Devices, 2nd ed., Wiley, Hoboken, 2009.
[43] E.F. Schubert, Light-Emitting Diodes, Cambridge University Press, San Jose, 2006.
[44] X. Chen, Z. Wu, S. Xu, L. Wang, R. Huang, Y. Han, et al., Nat. Commun. 6 (2015) 6088.
[45] Y. Lin, X. Ling, L. Yu, S. Huang, A.L. Hsu, Y.-H. Lee, et al., Nano Lett. 14 (2014) 5569–5576.
[46] F. Huser, T. Olsen, K.S. Thygesen,Phys. Rev. B 88 (2013), 245309.
[47] F. Wang, Y. Zhang, C. Tian, C. Girit, A. Zettl, M. Crommie, et al., Science 320 (2008) 206–209.
[48] V.N. Kotov, B. Uchoa, V.M. Pereira, F. Guinea, A.H. Castro Neto, Rev. Mod. Phys. 84 (2012) 1067–1125.
[49] J.T. Ye, Y.J. Zhang, R. Akashi, M.S. Bahramy, R. Arita, Y. Iwasa, Science 338 (2012) 1193–1196.
[50] J.T. Ye, S. Inoue, K. Kobayashi, Y. Kasahara, H.T. Yuan, H. Shimotani, et al., Nat. Mater. 9 (2009) 125.
[51] J.H. Chen, C. Jang, S. Adam, M.S. Fuhrer, E.D. Williams, M. Ishigami, Nat. Phys. 4 (2008) 377–381.
[52] P. Wallace, Phys. Rev. 71 (1947) 622–634.
[53] E. McCann, M. Koshino,Rep. Prog. Phys. 76 (2013), 056503.
[54] K.S. Novoselov, E. McCann, S.V. Morozov, V.I. Fal'ko, M.I. Katsnelson, U. Zeitler, et al., Nat. Phys. 2 (2006) 177–180.
[55] E. McCann, V.I. Fal'ko,Phys. Rev. Lett. 96 (2006), 086805.
[56] E. McCann,Phys. Rev. B 74 (2006), 161403.

[57] T. Ohta, A. Bostwick, T. Seyller, K. Horn, E. Rotenberg, Science 313 (2006) 951–954.
[58] E.V. Castro, K.S. Novoselov, S.V. Morozov, N.M.R. Peres, J.M.B.L. dos Santos, J. Nilsson, et al.,Phys. Rev. Lett. 99 (2007), 216802.
[59] J.B. Oostinga, H.B. Heersche, X.L. Liu, A.F. Morpurgo, L.M.K. Vandersypen, Nat. Mater. 7 (2008) 151–157.
[60] F.N. Xia, D.B. Farmer, Y.M. Lin, P. Avouris, Nano Lett. 10 (2010) 715–718.
[61] T. Taychatanapat, P. Jarillo-Herrero,Phys. Rev. Lett. 105 (2010), 166601.
[62] Y.B. Zhang, T.T. Tang, C. Girit, Z. Hao, M.C. Martin, A. Zettl, et al., Nature 459 (2009) 820–823.
[63] K.F. Mak, C.H. Lui, J. Shan, T.F. Heinz,Phys. Rev. Lett. 102 (2009), 256405.
[64] E.A. Henriksen, J.P. Eisenstein,Phys. Rev. B 82 (2010), 041412.
[65] A.F. Young, C.R. Dean, I. Meric, S. Sorgenfrei, H. Ren, K. Watanabe, et al.,Phys. Rev. B 85 (2012), 235458.
[66] L. Ju, L. Wang, T. Cao, T. Taniguchi, K. Watanabe, S.G. Louie, et al., Science 358 (2017) 907–910.
[67] B.N. Szafranek, G. Fiori, D. Schall, D. Neumaier, H. Kurz, Nano Lett. 12 (2012) 1324–1328.
[68] J. Yan, M.H. Kim, J.A. Elle, A.B. Sushkov, G.S. Jenkins, H.M. Milchberg, et al., Nat. Nanotechnol. 7 (2012) 472–478.
[69] O. Gunawan, Y.P. Shkolnikov, K. Vakili, T. Gokmen, E.P. De Poortere, M. Shayegan,Phys. Rev. Lett. 97 (2006), 186404.
[70] O. Gunawan, E.P. De Poortere, M. Shayegan,Phys. Rev. B 75 (2007), 081304.
[71] O. Gunawan, B. Habib, E.P. De Poortere, M. Shayegan,Phys. Rev. B 74 (2006), 155436.
[72] A. Rycerz, J. Tworzydło, C.W.J. Beenakker, Nat. Phys. 3 (2007) 172.
[73] K. Takashina, Y. Ono, A. Fujiwara, Y. Takahashi, Y. Hirayama,Phys. Rev. Lett. 96 (2006), 236801.
[74] K.F. Mak, K.L. He, J. Shan, T.F. Heinz, Nat. Nanotechnol. 7 (2012) 494–498.
[75] H.L. Zeng, J.F. Dai, W. Yao, D. Xiao, X.D. Cui, Nat. Nanotechnol. 7 (2012) 490–493.
[76] T. Cao, G. Wang, W. Han, H. Ye, C. Zhu, J. Shi, et al., Nat. Commun. 3 (2012) 887.
[77] D. Xiao, W. Yao, Q. Niu,Phys. Rev. Lett. 99 (2007), 236809.
[78] D. Xiao, G.-B. Liu, W. Feng, X. Xu, W. Yao,Phys. Rev. Lett. 108 (2012), 196802.
[79] R.V. Gorbachev, J.C.W. Song, G.L. Yu, A.V. Kretinin, F. Withers, Y. Cao, et al., Science 346 (2014) 448–451.
[80] M.Q. Sui, G.R. Chen, L.G. Ma, W.Y. Shan, D. Tian, K. Watanabe, et al., Nat. Phys. 11 (2015) 1027.
[81] Y. Shimazaki, M. Yamamoto, I.V. Borzenets, K. Watanabe, T. Taniguchi, S. Tarucha, Nat. Phys. 11 (2015) 1032.
[82] F. Amet, G. Finkelstein, Nat. Phys. 11 (2015) 989–990.
[83] K. Behnia, Nat. Nanotechnol. 7 (2012) 488.
[84] D. Culcer, A.L. Saraiva, B. Koiller, X. Hu, S. Das Sarma,Phys. Rev. Lett. 108 (2012), 126804.
[85] E.A. Laird, F. Pei, L.P. Kouwenhoven, Nat. Nanotechnol. 8 (2013) 565.
[86] D. Xiao, M.C. Chang, Q. Niu, Rev. Mod. Phys. 82 (2010) 1959–2007.
[87] I. Martin, Y.M. Blanter, A.F. Morpurgo,Phys. Rev. Lett. 100 (2008), 036804.
[88] F. Zhang, A.H. MacDonald, E.J. Mele, Proc. Natl. Acad. Sci. U. S. A. 110 (2013) 10546–10551.
[89] A. Vaezi, Y.F. Liang, D.H. Ngai, L. Yang, E.A. Kim,Phys. Rev. X 3 (2013), 021018.
[90] L. Ju, Z.W. Shi, N. Nair, Y.C. Lv, C.H. Jin, J. Velasco, et al., Nature 520 (2015) 650–655.
[91] J. Li, K. Wang, K.J. McFaul, Z. Zern, Y.F. Ren, K. Watanabe, et al., Nat. Nanotechnol. 11 (2016) 1060–1065.
[92] J. Li, R.X. Zhang, Z.X. Yin, J.X. Zhang, K. Watanabe, T. Taniguchi, et al., Science 362 (2018) 1149.
[93] C. Weisbuch, M. Nishioka, A. Ishikawa, Y. Arakawa, Phys. Rev. Lett. 69 (1992) 3314–3317.
[94] H. Haug, S.W. Koch, Quantum Theory of the Optical and Electronic Properties of Semiconductors, 4th ed., World Scientific, Singapore, 2004.
[95] S.W. Koch, M. Kira, G. Khitrova, H.M. Gibbs, Nat. Mater. 5 (2006) 523–531.
[96] A. Chernikov, T.C. Berkelbach, H.M. Hill, A. Rigosi, Y. Li, O.B. Aslan, et al.,Phys. Rev. Lett. 113 (2014), 076802.
[97] K.F. Mak, C. Lee, J. Hone, J. Shan, T.F. Heinz,Phys. Rev. Lett. 105 (2010), 136805.
[98] B. Zhu, X. Chen, X. Cui, Sci. Rep. 5 (2015) 9218.
[99] A. Ramasubramaniam,Phys. Rev. B 86 (2012), 115409.
[100] K. He, N. Kumar, L. Zhao, Z. Wang, K.F. Mak, H. Zhao, et al.,Phys. Rev. Lett. 113 (2014), 026803.
[101] X. Wang, A.M. Jones, K.L. Seyler, V. Tran, Y.C. Jia, H. Zhao, et al., Nat. Nanotechnol. 10 (2015) 517.
[102] L. Li, J. Kim, C.H. Jin, G.J. Ye, D.Y. Qiu, F.H. da Jornada, et al., Nat. Nanotechnol. 12 (2017) 21–25.
[103] G.W. Zhang, A. Chaves, S.Y. Huang, F.J. Wang, Q.X. Xing, T. Low, et al., Sci. Adv. 4 (2018).
[104] R.C. Miller, D.A. Kleinman, W.T. Tsang, A.C. Gossard, Phys. Rev. B 24 (1981) 1134–1136.
[105] P.W. Bridgman, J. Am. Chem. Soc. 36 (1914) 1344–1363.
[106] L. Li, Y.J. Yu, G.J. Ye, Q.Q. Ge, X.D. Ou, H. Wu, et al., Nat. Nanotechnol. 9 (2014) 372–377.
[107] F. Xia, H. Wang, Y. Jia, Nat. Commun. 5 (2014) 4458.
[108] H. Liu, A.T. Neal, Z. Zhu, Z. Luo, X.F. Xu, D. Tomanek, et al., ACS Nano 8 (2014) 4033–4041.
[109] S.P. Koenig, R.A. Doganov, H. Schmidt, A.H.C. Neto, B. Ozyilmaz,Appl. Phys. Lett. 104 (2014), 103106.
[110] A. Castellanos-Gomez, L. Vicarelli, E. Prada, J.O. Island, K.L. Narasimha-Acharya, S.I. Blanter, et al.,2D Mater 1 (2014), 025001.
[111] V. Tran, R. Soklaski, Y.F. Liang, L. Yang,Phys. Rev. B 89 (2014), 235319.
[112] X. Chen, Y. Wu, Z. Wu, Y. Han, S. Xu, L. Wang, et al., Nat. Commun. 6 (2015) 7315.
[113] L. Li, G.J. Ye, V. Tran, R. Fei, G. Chen, H. Wang, et al., Nat. Nanotechnol. 10 (2015) 608–613.
[114] J.S. Qiao, X.H. Kong, Z.X. Hu, F. Yang, W. Ji, Nat. Commun. 5 (2014) 4475.
[115] X. Chen, C. Chen, A. Levi, L. Houben, B.C. Deng, S.F. Yuan, et al., ACS Nano 12 (2018) 5003–5010.
[116] G. Long, D. Maryenko, J.Y. Shen, S.G. Xu, J.Q. Hou, Z.F. Wu, et al., Nano Lett. 16 (2016) 7768–7773.
[117] V. Tayari, N. Hemsworth, I. Fakih, A. Favron, E. Gaufres, G. Gervais, et al., Nat. Commun. 6 (2015) 7702.
[118] H. Yuan, X. Liu, F. Afshinmanesh, W. Li, G. Xu, J. Sun, et al., Nat. Nanotechnol. 10 (2014) 707–714.
[119] X. Chen, X. Lu, B. Deng, O. Sinai, Y. Shao, C. Li, et al., Nat. Commun. 8 (2017) 1672.
[120] A. Surrente, A.A. Mitioglu, K. Galkowski, W. Tabis, D.K. Maude, P. Plochocka,Phys. Rev. B 93 (2016), 121405.
[121] S. Das, W. Zhang, M. Demarteau, A. Hoffmann, M. Dubey, A. Roelofs, Nano Lett. 14 (2014) 5733–5739.
[122] L. Liang, J. Wang, W. Lin, B.G. Sumpter, V. Meunier, M. Pan, Nano Lett. 14 (2014) 6400–6406.
[123] X. Chen, L. Wang, Y. Wu, H. Gao, Y. Wu, G. Qin, et al.,2D Mater 3 (2016), 015012.
[124] M. Buscema, D.J. Groenendijk, S.I. Blanter, G.A. Steele, H.S.J. van der Zant, A. Castellanos-Gomez, Nano Lett. 14 (2014) 3347–3352.
[125] M. Buscema, D.J. Groenendijk, G.A. Steele, H.S.J. van der Zant, A. Castellanos-Gomez, Nat. Commun. 5 (2014) 4651.
[126] M. Engel, M. Steiner, P. Avouris, Nano Lett. 14 (2014) 6414–6417.
[127] N. Youngblood, C. Chen, S.J. Koester, M. Li, Nat. Photon. 9 (2015) 247–252.
[128] M.Q. Huang, M.L. Wang, C. Chen, Z.W. Ma, X.F. Li, J.B. Han, et al., Adv. Mater 28 (2016), 3481-+.
[129] W.S. Whitney, M.C. Sherrott, D. Jariwala, W.H. Lin, H.A. Bechtel, G.R. Rossman, et al., Nano Lett. 17 (2017) 78–84.
[130] R. Peng, K. Khaliji, N. Youngblood, R. Grassi, T. Low, M. Li, Nano Lett. 17 (2017) 6315–6320.
[131] J.W. Yang, S. Tran, J.S. Wu, S. Che, P. Stepanov, T. Taniguch, et al., Nano Lett. 18 (2018) 229–234.
[132] L. Li, F.Y. Yang, G.J. Ye, Z.C. Zhang, Z.W. Zhu, W.K. Lou, et al., Nat. Nanotechnol. 11 (2016) 592–596.
[133] H. Wang, X. Wang, F. Xia, L. Wang, H. Jiang, Q. Xia, et al., Nano Lett. 14 (2014) 6424–6429.
[134] W.N. Zhu, S. Park, M.N. Yogeesh, K.M. McNicholas, S.R. Bank, D. Akinwande, Nano Lett. 16 (2016) 2301–2306.
[135] A. Castellanos-Gomez, J. Phys. Chem. Lett. 6 (2015) 4280–4291.
[136] B. Deng, R. Frisenda, C. Li, X. Chen, A. Castellanos-Gomez, F. Xia,Adv. Opt. Mater. (2018), 1800365, DOI.
[137] A.J. Yang, D.W. Wang, X.H. Wang, D.Z. Zhang, N. Koratkar, M.Z. Rong, Nano Today 20 (2018) 13–32.
[138] H. Tian, J. Tice, R. Fei, V. Tran, X. Yan, L. Yang, et al., Nano Today 11 (2016) 763–777.
[139] H.Y. Guo, N. Lu, J. Dai, X.J. Wu, X.C. Zeng, J. Phys. Chem. C 118 (2014) 14051–14059.
[140] J. Dai, X.C. Zeng, J. Phys. Chem. Lett. 5 (2014) 1289–1293.
[141] Q.H. Liu, X.W. Zhang, L.B. Abdalla, A. Fazzio, A. Zunger, Nano Lett. 15 (2015) 1222–1228.
[142] Y. Li, S.X. Yang, J.B. Li, J. Phys. Chem. C 118 (2014) 23970–23976.
[143] J. Kim, S.S. Baik, S.H. Ryu, Y. Sohn, S. Park, B.G. Park, et al., Science 349 (2015) 723–726.
[144] B. Deng, V. Tran, Y. Xie, H. Jiang, C. Li, Q. Guo, et al., Nat. Commun. 8 (2017) 14474.
[145] Y. Liu, Q. Z, A. Carvalho, Y. Bao, H. Xu, S. Tan, et al., Nano Lett. 17 (2017) 1970–1977.
[146] S.L. Yan, Z.J. Xie, J.H. Chen, T. Taniguchi, K. Watanabe,Chin. Phys. Lett. 34 (2017), 047304.
[147] C. Lin, R. Grassi, T. Low, A.S. Helmyt, Nano Lett. 16 (2016) 1683–1689.
[148] C. Ataca, H. Şahin, S. Ciraci, J. Phys. Chem. C 116 (2012) 8983–8999.
[149] D.H. Keum, S. Cho, J.H. Kim, D.H. Choe, H.J. Sung, M. Kan, et al., Nat. Phys. 11 (2015) 482–486.
[150] S. Cho, S. Kim, J.H. Kim, J. Zhao, J. Seok, D.H. Keum, et al., Science 349 (2015) 625–628.
[151] R. Kappera, D. Voiry, S.E. Yalcin, B. Branch, G. Gupta, A.D. Mohite, et al., Nat. Mater. 13 (2014) 1128–1134.
[152] J. Zhu, Z. Wang, H. Yu, N. Li, J. Zhang, J. Meng, et al., J. Am. Chem. Soc. 139 (2017) 10216–10219.
[153] Y. Wang, J. Xiao, H.Y. Zhu, Y. Li, Y. Alsaid, K.Y. Fong, et al., Nature 550 (2017) 487.
[154] K.A.N. Duerloo, Y. Li, E.J. Reed, Nat. Commun. 5 (2014) 4214.
[155] Y.J. Yu, F.Y. Yang, X.F. Lu, Y.J. Yan, Y.H. Cho, L.G. Ma, et al., Nat. Nanotechnol. 10 (2015) 270–276.
[156] M.J. Hollander, Y. Liu, W.J. Lu, L.J. Li, Y.P. Sun, J.A. Robinson, et al., Nano Lett. 15 (2015) 1861–1866.
[157] G.X. Liu, B. Debnath, T.R. Pope, T.T. Salguero, R.K. Lake, A.A. Balandin, Nat. Nanotechnol. 11 (2016) 844–850.

[158] B. Sipos, A.F. Kusmartseva, A. Akrap, H. Berger, L. Forro, E. Tutis, Nat. Mater. 7 (2008) 960–965.
[159] B. Radisavljevic, A. Kis, Nat. Mater. 12 (2013) 815–820.
[160] B.W.H. Baugher, H.O.H. Churchill, Y.F. Yang, P. Jarillo-Herrero, Nano Lett. 13 (2013) 4212–4216.
[161] H.J. Chuang, X.B. Tan, N.J. Ghimire, M.M. Perera, B. Chamlagain, M.M.C. Cheng, et al., Nano Lett. 14 (2014) 3594–3601.
[162] S. Xu, Z. Wu, H. Lu, Y. Han, G. Long, X. Chen, et al.,2D Mater 3 (2016), 021007.
[163] N.R. Pradhan, A. McCreary, D. Rhodes, Z.G. Lu, S.M. Feng, E. Manousakis, et al., Nano Lett. 15 (2015) 8377–8384.
[164] N. Gillgren, D. Wickramaratne, Y. Shi, T. Espiritu, J. Yang, J. Hu, et al.,2D Mater 2 (2015), 011001.
[165] S.V. Kravchenko, G.V. Kravchenko, J.E. Furneaux, V.M. Pudalov, M. D'Iorio, Phys. Rev. B 50 (1994) 8039–8042.
[166] S. He, X.C. Xie, Phys. Rev. Lett. 80 (1998) 3324–3327.
[167] M.J. Manfra, E.H. Hwang, S. Das Sarma, L.N. Pfeiffer, K.W. West, A.M. Sergent,Phys. Rev. Lett. 99 (2007), 236402.
[168] A. Shashkin, V. Dolgopolov, G. Kravchenko, M. Wendel, R. Schuster, J. Kotthaus, et al., Phys. Rev. Lett. 73 (1994) 3141–3144.
[169] H. Yang, S.W. Kim, M. Chhowalla, Y.H. Lee, Nat. Phys. 13 (2017) 931–937.
[170] Y. Meir, Phys. Rev. Lett. 83 (1999) 3506–3509.
[171] S. Adam, S. Cho, M.S. Fuhrer, S. Das Sarma,Phys. Rev. Lett. 101 (2008), 046404.
[172] A. Punnoose, A.M. Finkel'stein, Science 310 (2005) 289–291.
[173] B.H. Moon, J.J. Bae, M.-K. Joo, H. Choi, G.H. Han, H. Lim, et al., Nat. Commun. 9 (2018) 2052.
[174] J.M. Lu, O. Zheliuk, I. Leermakers, N.F.Q. Yuan, U. Zeitler, K.T. Law, et al., Science 350 (2015) 1353–1357.
[175] Y. Saito, Y. Nakamura, M.S. Bahramy, Y. Kohama, J. Ye, Y. Kasahara, et al., Nat. Phys. 12 (2015) 144.
[176] D. Costanzo, H.J. Zhang, B.A. Reddy, H. Berger, A.F. Morpurgo, Nat. Nanotechnol. 13 (2018) 483–488.
[177] D. Costanzo, S. Jo, H. Berger, A.F. Morpurgo, Nat. Nanotechnol. 11 (2016) 339.
[178] S. Jo, D. Costanzo, H. Berger, A.F. Morpurgo, Nano Lett. 15 (2015) 1197–1202.
[179] J. Lu, O. Zheliuk, Q. Chen, I. Leermakers, N.E. Hussey, U. Zeitler, et al., Proc. Natl. Acad. Sci. U. S. A. 115 (2018) 3551–3556.
[180] W. Shi, J. Ye, Y. Zhang, R. Suzuki, M. Yoshida, J. Miyazaki, et al., Sci. Rep. 5 (2015) 12534.
[181] K.F. Mak, K.L. McGill, J. Park, P.L. McEuen, Science 344 (2014) 1489–1492.
[182] N. Nagaosa, J. Sinova, S. Onoda, A.H. MacDonald, N.P. Ong, Rev. Mod. Phys. 82 (2010) 1539–1592.
[183] J. Lee, K.F. Mak, J. Shan, Nat. Nanotechnol. 11 (2016) 421.
[184] Z. Wu, B.T. Zhou, G.B. Liu, J. Lin, T. Han, L. An, et al., Nat. Commun. 10 (2019) 611.
[185] Y.T. Hung, Y. Camsari, S. Zhang, P. Upadhyaya, Z. Chen, arXiv 1805 (06054) (2018), DOI.
[186] M.N. Ali, J. Xiong, S. Flynn, J. Tao, Q.D. Gibson, L.M. Schoop, et al., Nature 514 (2014) 205.
[187] I. Pletikosic, M.N. Ali, A.V. Fedorov, R.J. Cava, T. Valla,Phys. Rev. Lett. 113 (2014), 216601.
[188] L. Wang, I. Gutierrez-Lezama, C. Barreteau, N. Ubrig, E. Giannini, A.F. Morpurgo, Nat. Commun. 6 (2015) 8892.
[189] F.X. Xiang, M. Veldhorst, S.X. Dou, X.L. Wang, Epl-Europhys. Lett. 112 (2015) 37009.
[190] Y.F. Zhao, H.W. Liu, J.Q. Yan, W. An, J. Liu, X. Zhang, et al.,Phys. Rev. B 92 (2015), 041104.
[191] P.L. Cai, J. Hu, L.P. He, J. Pan, X.C. Hong, Z. Zhang, et al.,Phys. Rev. Lett. 115 (2015), 057202.
[192] Z.W. Zhu, X. Lin, J. Liu, B. Fauque, Q. Tao, C.L. Yang, et al.,Phys. Rev. Lett. 114 (2015), 176601.
[193] L.R. Thoutam, Y.L. Wang, Z.L. Xiao, S. Das, A. Luican-Mayer, R. Divan, et al.,Phys. Rev. Lett. 115 (2015), 046602.
[194] L. Wang, I. Gutierrez-Lezama, C. Barreteau, D.K. Ki, E. Giannini, A.F. Morpurgo,Phys. Rev. Lett. 117 (2016), 176601.
[195] S. Jia, S.Y. Xu, M.Z. Hasan, Nat. Mater. 15 (2016) 1140–1144.
[196] A.A. Soluyanov, D. Gresch, Z.J. Wang, Q.S. Wu, M. Troyer, X. Dai, et al., Nature 527 (2015) 495–498.
[197] Y. Wu, D.X. Mou, N.H. Jo, K.W. Sun, L.N. Huang, S.L. Bud'ko, et al.,Phys. Rev. B 94 (2016), 121113.
[198] F.Y. Bruno, A. Tamai, Q.S. Wu, I. Cucchi, C. Barreteau, A. de la Torre, et al.,Phys. Rev. B 94 (2016), 121112.
[199] C.L. Wang, Y. Zhang, J.W. Huang, S.M. Nie, G.D. Liu, A.J. Liang, et al.,Phys. Rev. B 94 (2016), 241119.
[200] P. Li, Y. Wen, X. He, Q. Zhang, C. Xia, Z.-M. Yu, et al., Nat. Commun. 8 (2017) 2150.
[201] Y. Wang, E. Liu, H. Liu, Y. Pan, L. Zhang, J. Zeng, et al., Nat. Commun. 7 (2016) 13142.
[202] X.F. Qian, J.W. Liu, L. Fu, J. Li, Science 346 (2014) 1344–1347.
[203] F.P. Zheng, C.Y. Cai, S.F. Ge, X.F. Zhang, X. Liu, H. Lu, et al., Adv. Mater 28 (2016) 4845–4851.
[204] Z.Y. Fei, T. Palomaki, S.F. Wu, W.J. Zhao, X.H. Cai, B.S. Sun, et al., Nat. Phys. 13 (2017) 677.
[205] S.F. Wu, V. Fatemi, Q.D. Gibson, K. Watanabe, T. Taniguchi, R.J. Cava, et al., Science 359 (2018) 76–79.
[206] S.J. Tang, C.F. Zhang, D. Wong, Z. Pedramrazi, H.Z. Tsai, C.J. Jia, et al., Nat. Phys. 13 (2017) 683.
[207] L. Peng, Y. Yuan, G. Li, X. Yang, J.-J. Xian, C.-J. Yi, et al., Nat. Commun. 8 (2017) 659.
[208] Y.-H. Song, Z.-Y. Jia, D. Zhang, X.-Y. Zhu, Z.-Q. Shi, H. Wang, et al., Nat. Commun. 9 (2018) 4071.
[209] Z.-Y. Jia, Y.-H. Song, X.-B. Li, K. Ran, P. Lu, H.-J. Zheng, et al.,Phys. Rev. B 96 (2017), 041108.
[210] E. Sajadi, T. Palomaki, Z. Fei, W. Zhao, P. Bement, C. Olsen, et al., Science (2018), http://dx.doi.org/10.1126/science.aar4642.
[211] V. Fatemi, S. Wu, Y. Cao, L. Bretheau, Q.D. Gibson, K. Watanabe, et al., Science (2018), http://dx.doi.org/10.1126/science.aar4642.
[212] Z.Y. Fei, W.J. Zhao, T.A. Palomaki, B.S. Sun, M.K. Miller, Z.Y. Zhao, et al., Nature 560 (2018) 336.
[213] N.D. Mermin, H. Wagner, Phys. Rev. Lett. 17 (1966) 1133.
[214] B. Huang, G. Clark, E. Navarro-Moratalla, D.R. Klein, R. Cheng, K.L. Seyler, et al., Nature 546 (2017) 270.
[215] C. Gong, L. Li, Z.L. Li, H.W. Ji, A. Stern, Y. Xia, et al., Nature 546 (2017) 265.
[216] Y. Deng, Y. Yu, Y. Song, J. Zhang, N.Z. Wang, Z. Sun, et al., Nature 563 (2018) 94–99.
[217] Z.Y. Fei, B. Huang, P. Malinowski, W.B. Wang, T.C. Song, J. Sanchez, et al., Nat. Mater. 17 (2018) 778.
[218] T.C. Song, X.H. Cai, M.W.Y. Tu, X.O. Zhang, B.V. Huang, N.P. Wilson, et al., Science 360 (2018) 1214.
[219] D.R. Klein, D. MacNeill, J.L. Lado, D. Soriano, E. Navarro-Moratalla, K. Watanabe, et al., Science 360 (2018) 1218.
[220] Z. Wang, I. Gutierrez-Lezama, N. Ubrig, M. Kroner, M. Gibertini, T. Taniguchi, et al., Nat. Commun. 9 (2018) 2516.
[221] B. Huang, G. Clark, D.R. Klein, D. MacNeill, E. Navarro-Moratalla, K.L. Seyler, et al., Nat. Nanotechnol. 13 (2018) 544.
[222] S.W. Jiang, L.Z. Li, Z.F. Wang, K.F. Mak, J. Shan, Nat. Nanotechnol. 13 (2018) 549.
[223] N. Sivadas, S. Okamoto, X. Xu, C.J. Fennie, D. Xiao, Nano Lett. 18 (2018) 7658–7664.
[224] Z. Wang, T. Zhang, M. Ding, B. Dong, Y. Li, M. Chen, et al., Nat. Nanotechnol. 13 (2018) 554–559.
[225] C. Tan, J. Lee, S.G. Jung, T. Park, S. Albarakati, J. Partridge, et al., Nat. Commun. 9 (2018) 1554.
[226] Q. Li, M.M. Yang, C. Gong, R.V. Chopdekar, A.T. N'Diaye, J. Turner, et al., Nano Lett. 18 (2018) 5974–5980.
[227] G.D. Nguyen, J. Lee, T. Berlijn, Q. Zou, S.M. Hus, J. Park, et al.,Phys. Rev. B 97 (2018), 014425.
[228] Z. Wang, D. Sapkota, T. Taniguchi, K. Watanabe, D. Mandrus, A.F. Morpurgo, Nano Lett. 18 (2018) 4303–4308.
[229] J.-U. Lee, S. Lee, J.H. Ryoo, S. Kang, T.Y. Kim, P. Kim, et al., Nano Lett. 16 (2016) 7433–7438.
[230] X. Li, X. Wu, J. Yang, J. Am. Chem. Soc. 136 (2014) 11065–11069.
[231] B.L. Chittari, Y. Park, D. Lee, M. Han, A.H. MacDonald, E. Hwang, et al.,Phys. Rev. B 94 (2016), 184428.
[232] H. Taniguchi, S. Suzuki, T. Arakawa, H. Yoshida, Y. Niimi, K. Kobayashi, AIP Adv. 8 (2018), 025010.
[233] T. Kida, A. Okutani, H. Yoshida, M. Hagiwara, Phys. Procedia 75 (2015) 647–652.
[234] L. Hu, X.J. Wu, J.L. Yang, Nanoscale 8 (2016) 12939–12945.
[235] D.J. O'Hara, T. Zhu, A.H. Trout, A.S. Ahmed, Y.K. Luo, C.H. Lee, et al., Nano Lett. 18 (2018) 3125–3131.
[236] M. Bonilla, S. Kolekar, Y. Ma, H.C. Diaz, V. Kalappattil, R. Das, et al., Nat. Nanotechnol. 13 (2018) 289–293.
[237] T. Miyadai, K. Kikuchi, H. Kondo, S. Sakka, M. Arai, Y. Ishikawa, J. Phys. Soc. Jpn. 52 (1983) 1394–1401.
[238] Y. Togawa, T. Koyama, K. Takayanagi, S. Mori, Y. Kousaka, J. Akimitsu, et al.,Phys. Rev. Lett. 108 (2012), 107202.
[239] N.J. Ghimire, M.A. McGuire, D.S. Parker, B. Sipos, S. Tang, J.Q. Yan, et al.,Phys. Rev. B 87 (2013), 104403.
[240] L. Wang, N. Chepiga, D.K. Ki, L. Li, F. Li, W. Zhu, et al.,Phys. Rev. Lett. 118 (2017), 257203.
[241] D.A. Bandurin, A.V. Tyurnina, G.L. Yu, A. Mishchenko, V. Zólyomi, S.V. Morozov, et al., Nat. Nanotechnol. 12 (2016) 223.
[242] F. Li, X. Liu, Y. Wang, Y. Li, J. Mater. Chem. C 4 (2016) 2155–2159.
[243] Y. Zhou, D. Wu, Y. Zhu, Y. Cho, Q. He, X. Yang, et al., Nano Lett. 17 (2017) 5508–5513.
[244] W. Huang, L. Gan, H. Li, Y. Ma, T. Zhai, CrystEngComm 18 (2016) 3968–3984.
[245] Y. Cui, Z. Zhou, T. Li, K. Wang, J. Li, Z. Wei,Adv. Funct. Mater. 0 (2019), 1900040.
[246] R. Fei, W. Li, J. Li, L. Yang,Appl. Phys. Lett. 107 (2015), 173104.
[247] Y. Cao, V. Fatemi, S. Fang, K. Watanabe, T. Taniguchi, E. Kaxiras, et al., Nature 556 (2018) 43.
[248] J. Bardeen, L.N. Cooper, J.R. Schrieffer, Phys. Rev. 108 (1957) 1175–1204.
[249] C. Jin, J. Kim, J. Suh, Z. Shi, B. Chen, X. Fan, et al., Nat. Phys. 13 (2016) 127.
[250] C. Chen, X. Chen, H. Yu, Y. Shao, Q. Guo, B. Deng, et al., ACS Nano 13 (2019) 552–559.
[251] J.-H. Lee, E.K. Lee, W.-J. Joo, Y. Jang, B.-S. Kim, J.Y. Lim, et al., Science 344 (2014) 286–289.
[252] J.S. Lee, S.H. Choi, S.J. Yun, Y.I. Kim, S. Boandoh, J.-H. Park, et al., Science 362 (2018) 817–821.
[253] K. Kang, S. Xie, L. Huang, Y. Han, P.Y. Huang, K.F. Mak, et al., Nature 520 (2015) 656.

[254] C. Li, Y. Wu, B. Deng, Y. Xie, Q. Guo, S. Yuan, et al.,Adv. Mater 30 (2018), 1703748.

Xiaolong Chen received his B.S. degree from University of Science and Technology of China (USTC) in 2010, and Ph.D. degree from Hong Kong University of Science and Technology in 2014, respectively. Then he carried out his postdoctoral research at the University of Cambridge and Yale University. He is currently an assistant professor at Southern University of Science and Technology, Shenzhen, China. His field of interests is two-dimensional material device physics, electronics, and optoelectronics.

Zishu Zhou received his bachelor degree in Opto-Electronic Information Science and Engineering from Nanjing Tech University in 2017. He is currently a master student in the Institute of Advanced Materials (IAM) at Nanjing Tech University. His field of interest is the opto-electronic properties and quantum transport of two-dimensional materials.

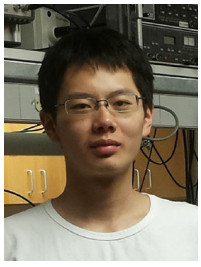

Bingchen Deng is currently a Ph.D. student at Yale University. In 2014, He received his B.S. degree in physics from University of Science and Technology of China (USTC). Then he joined Prof. Fengnian Xia's research group of Laboratory of Emerging Materials and Devices. His research interests include low-dimensional material electronics, optoelectronics, plasmonics, and valleytronics.

Zefei Wu received his B.S. degree from University of Science and Technology of China in 2010, and Ph.D. degree in Physics from the Hong Kong University of Science and Technology (HKUST) in 2014. He worked as a postdoctoral researcher in HKUST (2014–2016). Then he moved to Beijing Institute of Technology and worked as an assistant professor (2016–2017). He is now a visiting scholar in the Department of Physics at HKUST. His current research interest is in the investigation of novel electronic and valleytronic properties in 2D quantum materials.

Fengnian Xia received the B.E. degree with highest honor in electronics engineering from Tsinghua University, Beijing, China and Ph.D. degree in electrical engineering from Princeton University, Princeton, NJ, USA. He held postdoc, engineer and research staff positions in IBM Thomas J. Watson research center in Yorktown Heights, NY, USA from 2005 to 2013. He joined Yale University in 2013 as an assistant professor and he is currently the Barton L. Weller associate professor in engineering and science at Department of Electrical Engineering. He explores the light-matter interaction and quantum transport in low-dimensional quantum materials and identifies their potential applications in computing, flexible electronics, imaging, optical communications, and energy harvesting.

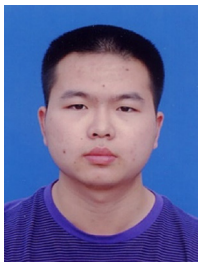

Yi Cao received his bachelor degree in Opto-Electronic Information Science and Engineering from Nanjing Tech University in 2017. He is currently a master student in the Institute of Advanced Materials (IAM) at Nanjing Tech University. His field of interest is the magnetic properties of two-dimensional materials, in particular the ones with topological spin texture.

Le Zhang received her B.S. and M.S. degree from Shandong University in 2015 and 2018, respectively. She is currently a PhD student at Southern University of Science and Technology, Shenzhen, China. Her research interests include low-dimensional material synthesis, property characterization, and device fabrication.

Wei Huang is an academician of the Chinese Academy of Sciences, foreign academician of the Russian Academy of Sciences, foreign member of the ASEAN Academy of Engineering and Technology, fellow of the Royal Society of Chemistry and fellow of the Optical Society of America. He received his BSc, MSc and PhD from Peking University, and then carried out his postdoctoral research at the National University of Singapore, where he co-founded the Institute of Materials Research and Engineering. He is currently the deputy president and provost of Northwestern Polytechnical University, China. His research interests include polymer sciences, organic/plastic/flexible electronics, nanoelectronics and bioelectronics.

Ning Wang obtained his PhD (1990) degree in materials physics from the University of Science and Technology, Beijing. During 1989–1993, he worked at the Institute for Metal Physics, Goettingen University and the Fritz-Haber-Institute of the Max-Planck Society, Berlin, Germany. In 1993, he joined the Physics Department of the Hong Kong University of Science and Technology (HKUST). Professor Wang is currently Chair Professor of Physics, Director of Center for Quantum Materials and Director of Materials Characterization & Preparation Facility at HKUST. His research interests include fundamental issues of nanostructure and nano-device technology, quantum transport of two-dimensional structures, and high-resolution transmission electron microscopy.

Lin Wang received her bachelor degree in physics from Wuhan University in 2009, and Ph.D degree from the Hong Kong University of Science and Technology in 2013. She is currently a professor in Nanjing Tech University. She is mainly focused on the synthesis and the (opto-)electronic properties of two-dimensional materials.